



A new Martian meteorite from Oman: Mineralogy, petrology, and shock metamorphism of olivine-phyric basaltic shergottite Sayh al Uhaymir 150

E. L. WALTON^{1*}, J. G. SPRAY¹, and R. BARTOSCHEWITZ²

¹Planetary and Space Science Centre, Department of Geology, University of New Brunswick,
Bailey Drive, Fredericton, New Brunswick E3B 5A3, Canada

²Meteorite Laboratory, Lehmweg 53, D-38518 Gifhorn, Germany

*Corresponding author. E-mail: j5rng@unb.ca

(Received 22 March 2005; revision accepted 17 June 2005)

Abstract—The Sayh al Uhaymir (SaU) 150 meteorite was found on a gravel plateau, 43.3 km south of Ghaba, Oman, on October 8, 2002. Oxygen isotope ($\delta^{17}\text{O}$ 2.78; $\delta^{18}\text{O}$ 4.74), CRE age (~1.3 Ma), and noble gas studies confirm its Martian origin. SaU 150 is classified as an olivine-phyric basalt, having a porphyritic texture with olivine macrocrysts set in a finer-grained matrix of pigeonite and interstitial maskelynite, with minor augite, spinel, ilmenite, merrillite, pyrrhotite, pentlandite, and secondary (terrestrial) calcite and iron oxides. The bulk rock composition, in particular mg (68) [molar Mg/(Mg + Fe) \times 100], Fe/Mn (37.9), and Na/Al (0.22), are characteristic of Martian meteorites.

Based on mineral compositions, cooling rates determined from crystal morphology, and crystal size distribution, it is deduced that the parent magma formed in a steady-state growth regime (magma chamber) that cooled at <2 °C/hr. Subsequent eruption as a thick lava flow or hypabyssal intrusion entrained a small fraction of xenocrystic olivine and gave rise to a magmatic foliation, with slow cooling allowing for near homogenization of igneous minerals.

SaU 150 experienced an equilibration shock pressure of 33–45 GPa in a single impact event. Post-shock heat gave rise to localized melting (~11 vol%). Larger volume melts remained fluid after pressure release and crystallized dendritic olivine and pyroxene with fractal dimensions of 1.80–1.89 and 1.89–1.95, respectively, at $-\Delta T > 70$ –365 °C.

SaU 150 is essentially identical to SaU 005/094, all representing samples of the same fall that are similar to, but distinct from, the DaG shergottites.

INTRODUCTION

The Martian meteorite Sayh al Uhaymir (SaU) 150, weighing 107.7 g, was found on a gravel plateau of Miocene freshwater limestone, 43.3 km south of Ghaba, Oman, by one of the authors (RB) and his son on October 8, 2002 (Fig. 1). The stone was initially described in an abstract by Bartoschewitz and Appel (2003) as a porphyritic basalt with olivine phenocrysts set in a matrix of pyroxene and feldspathic glass (see also Russell et al. 2003). A small patch (~1 cm²) of black-brown fusion crust remains intact on the exterior of the stone. The oxygen isotopic composition of $\delta^{17}\text{O} + 2.78$ and $\delta^{18}\text{O} + 4.74$, measured by R. N. Clayton (Russell et al. 2003), plots close to the fractionation line defined by other Martian meteorites (Clayton and Mayeda 1996; Franchi et al. 1999), confirming its Martian origin. SaU 150 is one of ten meteorites encompassing 17 specimens found in a strewn field approximately 3.6×2 km: SaU 005 (3

fragments totalling 1344 g; Grossman 2000), SaU 008 (2 fragments totalling 8579 g; Grossman 2000), SaU 051 (456 g; Grossman and Zipfel 2001), SaU 094 (223.3 g; Grossman and Zipfel 2001), SaU 060 (42.28 g; Russell et al. 2002), SaU 090 (94.84 g; Russell et al. 2002), SaU 120 (75 g; Russell et al. 2003), SaU 125 (31.7 g; Russell et al. 2004), and SaU 130 (4 fragments totalling 278 g; Russell et al. 2004), excluding several non-described fragments. All paired meteorites have basaltic textures with olivine macrocrysts and are similar in their texture, mineralogy, chemistry, and exposure age to the Dar al Gani (DaG) 476/489/735/670/876/975 shergottites, recovered from a strewn field in Libya, with the exception of less pronounced weathering in the SaU meteorites (Croizat and Wadhwa 2001). Cosmic ray exposure (CRE) ages for SaU 150, based on the stable noble gas isotopes ³He, ²¹Ne, and ³⁸Ar, are 1.31 Ma, 1.28 Ma, and 0.66 Ma, respectively, as reported by Park et al. (2004). The CRE ages overlap with those previously reported for SaU 005/060 (Park et al. 2003),



Fig. 1. Field photographs of the SaU 150 meteorite as found on a gravel plateau of freshwater limestone. a) The dark color of the meteorite, in addition to its luster, makes it easy to recognize as exotic to the surrounding landscape. b) SaU 150 as found with global positioning system (GPS) for scale showing the location at $20^{\circ}59'31.3''\text{N}$, $57^{\circ}19'11.7''\text{E}$.

showing pairing between meteorite samples. A K-Ar apparent age of 0.69 ± 0.08 Ga (Park et al. 2004) lacks context because the analyzed whole rock samples probably include host rock minerals, and in addition, shock melts containing a trapped Martian atmospheric component (e.g., Bogard and Garrison 1999). Ratios of $(^{40}\text{Ar})/(^{36}\text{Ar})_t$ and $^{129}\text{Xe}/^{132}\text{Xe}$ from higher temperature extractions are characteristic of a trapped Martian atmospheric component (Ar: 1383 ± 305 at 1300°C ; Xe: 1.314 ± 0.0604 at 1750°C).

There exists a vast literature related to Martian meteorites (over 1800 publications cited in the Mars Meteorite Compendium alone; Meyer 2004), and, in light of a Mars sample return mission within the decade, a similar effort to describe such material can be expected. The increase in Martian meteorite recovery—20 meteorites in the last two

decades—is mainly the result of the intensive search for meteorites, particularly in North African and Arabian deserts and Antarctica. At present, there is a need for comprehensive descriptions of Martian samples to keep the database current as new material is discovered. The Mars Meteorite Compendium (Meyer 2004) represents the ongoing results of such an effort; however, there still exist new Martian meteorite paired fragments whose descriptions are restricted to non-refereed abstracts.

Here we present a detailed study of the petrology, mineralogy, and shock metamorphism of the SaU 150 Martian meteorite with implications for its igneous petrogenesis, impact history, and evaluation of its relationship to other paired and non-paired shergottites (basaltic and olivine-phyric basaltic). In addition, a novel approach to quantifying crystal morphology has been applied for the first time to two Martian meteorites (SaU 150 and DaG 476) in order to compare their crystallinity and post-shock cooling history. Using the texture correlation technique (Fowler 1995), the fractal dimension of disequilibrium crystals present in large mm-size melt pockets has been determined. These melt pockets are distinct from shock-related melt veins and melt pockets described in other Martian basalts (e.g., Zagami). Investigation of these melt pockets may help to shed light on mechanisms responsible for their formation.

ANALYTICAL METHODS

Two doubly polished thin sections of SaU 150 and one crystal bond-mounted ultrathin section of DaG 476 were initially studied by transmitted and reflected light microscopy. Backscattered electron images (BSE), X-ray maps, and quantitative analyses were obtained using a JEOL 6400 digital scanning electron microscope (SEM) equipped with an EDAX Phoenix X-ray microanalysis system with a Sapphire Si(Li) detector and Genesis microanalysis software, and a JEOL 733 electron microprobe (EMP) equipped with four wavelength dispersive (WDS) spectrometers. SEM analyses were determined at count times of 60 sec, beam operating conditions of 15 kV and 1.5 nA, and a working distance of 14 mm. Analyses were calibrated using a multi-element standards block (type 202-52) produced by the C. M. Taylor Corporation of Sunnyvale, California, USA. Where alkali mobility was not deemed problematic, EMP conditions of 15 kV accelerating voltage, 30 nA beam current, and an approximate beam diameter of 1–2 μm , were deployed. Single spot analysis was used to determine the composition of individual host rock minerals. Raster scans in separate areas of $20 \mu\text{m} \times 26 \mu\text{m}$ at $5000\times$ magnification were used to determine the bulk composition of melt pockets. Energy-dispersive spectrometry (EDS) was used because of its ability to minimize alkali metal migration (e.g., Spray and Rae 1995). X-ray elemental maps were acquired on the same SEM at 15 kV accelerating voltage, 25 nA beam current, at a

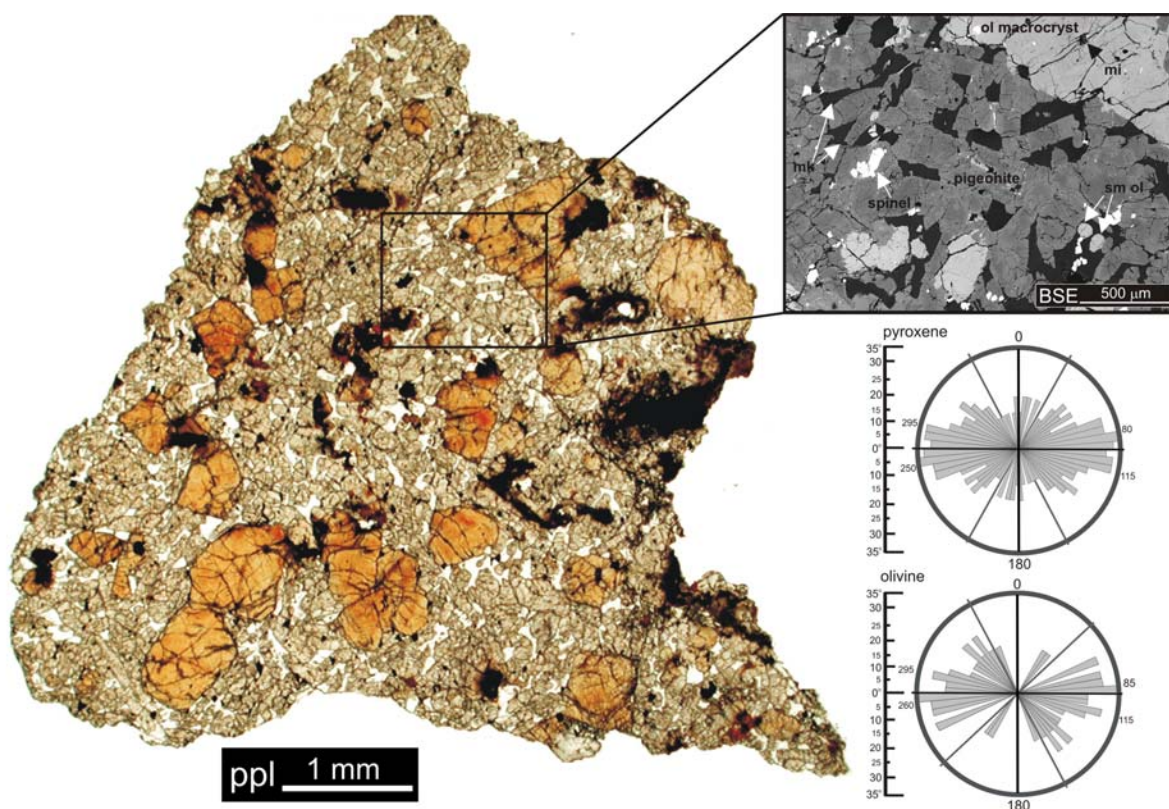


Fig. 2. Plane-polarized light (ppl) image of SaU 150 in thin section. Olivine macrocrysts (large, brown crystals) are embedded in a finer-grained groundmass of pyroxene and interstitial maskelynite (see higher magnification BSE image). Black, irregularly-shaped enclaves dispersed throughout the groundmass and located at edges of olivine macrocrysts are melt pockets of variable crystallinity. Measurement of the orientation of the longest dimension of 352 prismatic pyroxene and 34 olivine crystals show a shape-preferred orientation of both phases, illustrated in the rose diagrams. mk = maskelynite, mi = melt inclusion, sm = small, ol = olivine.

processor time constant of 3.2 sec, and a resolution of 512×400 pixels. SEM BSE images and the image analysis software ImageJ were used to determine the modal abundance of constituent phases and textural characteristics of the meteorite. A texture correlation program, written in Visual Basic, was used to determine the fractal dimension of dendritic crystals using BSE images converted to binary maps.

RESULTS

Petrography and Mineral Composition

SaU 150 has an olivine-porphyritic texture with large (up to 3 mm-size) zoned olivine crystals or crystal clusters embedded in a finer-grained groundmass consisting primarily of pyroxene (pigeonite and augite), unzoned olivine, and interstitial plagioclase (now a diaplectic plagioclase glass, maskelynite) (Fig. 2). Compositions of clinopyroxenes, olivine, and maskelynite are illustrated in Fig. 3.

Mineral modes for the two sections have been determined by manual point counting ($n = 4000$ on both sections), and image analysis, showing good agreement

between the two methods (Table 1). The mineral mode (in vol%) is 49.8–54.6% clinopyroxene, 17.2–23.1% olivine, 13.8–15.5% maskelynite, 1.6–3.8% opaques, 0.2–0.3% primary melt inclusions, and 10.2–11.3% melt pockets. Discrepancies in mineral abundances between the two studied sections are attributed to the heterogeneity in volume and distribution of melt pockets. Compared to other Martian meteorites, SaU 150 contains a similar amount of olivine, maskelynite, and clinopyroxene, but does not contain orthopyroxene, unlike all other olivine-phyric basalts, which are enstatite-bearing (Zipfel et al. 2000; Folco et al. 2000; McSween and Jarosewich 1983; Irving et al. 2004; Greshake et al. 2004). Excluding melt pockets that overprint igneous textures, the mineral mode and texture can be used to classify SaU 150 as an olivine basalt.

Olivine

Three chemically and morphologically distinct olivine types are distinguished: 1) large (550–3200 μm in diameter), subhedral single crystal or glomerophytic olivine macrocrysts, zoned from magnesian cores ($\text{Fo}_{64.5-70.0}$) to slightly more fayalitic rims ($\text{Fo}_{62.7-66.3}$), 2) smaller (50–400 μm in diameter), euhedral to subrounded, slightly more

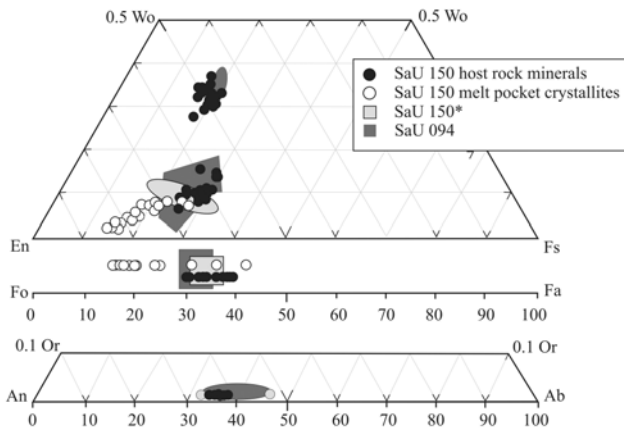


Fig. 3. Compositional data for pyroxene, olivine, and maskelynite in SaU 150 (this work; Bartoschewitz and Appel 2003) and SaU 094 (Gnos et al. 2002). All data reported in mol%. Composition of melt pocket crystallites are shown for comparison.

Fe-rich olivine grains that typically show little compositional variation from core to rim ($\text{Fo}_{59.8-62.8}$), and 3) dendritic, zoned olivine formed exclusively in large mm-size melt pockets (see Melt Pockets section).

Coarser-grained olivine macrocrysts have aspect ratios varying from $\sim 1.1-2.1$. The coarsest mm-size olivine macrocrysts contain embayments of groundmass material. The trend of increasing Fo content of core compositions with increasing grain size is observed in $\sim 95\%$ of zoned grains. This trend, however, is not always the case. Approximately 5% of olivine macrocrysts show reverse zoning with rims having slightly higher Fo contents compared to their core compositions. Large olivine macrocrysts with distinctly Mg-rich cores, $\text{Fo}_{>74}$ (up to Fo_{84} in Yamato-980459) (Greshake et al. 2004), are not present in the studied sections. Olivine shows relatively high Ca contents, 0.1–0.3 wt% CaO, consistent with analyses of olivine in other Martian meteorites (e.g., Folco et al. 2000). The most Fe-rich rims of large olivine macrocrysts overlap in composition with those of the smaller olivine grains. Zoning is most pronounced in the outer 1–2 microns of the crystal.

Smaller olivines are subrounded and have an aspect ratio of ~ 1 . Polyhedral crystals with well-defined faces are typically slightly elongated, yielding aspect ratios as high as 2.6. Image analysis has revealed a shape-preferred orientation of prismatic pyroxene, and, less obviously, of olivine, which is apparent in a rose diagram (Fig. 2).

Pyroxenes

Groundmass pyroxene is dominantly pigeonite. The preponderance of pigeonite over augite and orthopyroxene is observed in other olivine-phyric shergottites, with the exception of Northwest Africa (NWA) 1068 and Yamato-980459 (McSween and Jarosewich 1983; Barrat et al. 2002; Zipfel et al. 2000; Mikouchi et al. 2001; Greshake et al.

2004). Prismatic grains have a mean width of 98 μm (8–115 μm) and a mean length of 348 μm (182–790 μm), with aspect ratios as high as 8.3. Euhedral basal sections have a mean apparent diameter of 131 μm (33–375 μm) forming 6- to 8-sided sections or subrounded anhedral grains. Groundmass augite forms grains distinct from pigeonite (typically $<120 \mu\text{m}$ diameter).

Examination of pyroxenes at high magnification using backscattered electron imaging revealed no evidence for exsolution at the micron scale. Groundmass pigeonite ranges from $\text{En}_{56.7-69.9}\text{Fs}_{22.7-34.9}\text{Wo}_{6.6-17.6}$, and augite from $\text{En}_{46.5-54.5}\text{Fs}_{15-19.3}\text{Wo}_{27.6-37.1}$. Compositional zoning in pigeonite and augite is normal, but less pronounced than reported for other olivine-phyric shergottites (e.g., DaG 476, Mikouchi et al. 2001; NWA 1068, Barrat et al. 2002). Mg numbers for pigeonite range from 62–75. Augite shows slightly higher values of 72–77. Variations in TiO_2 , MnO, Al_2O_3 , and Cr_2O_3 abundances relative to mg are shown in Fig. 4. Pigeonite and augite show similar trends. TiO_2 increases with decreasing mg, with steep slopes at the lowest mg, from 62–64 for pigeonite, and from mg 72–74 for augite. Likewise, MnO concentrations increase over the range of mg. Al_2O_3 and Cr_2O_3 behave similarly, both showing a decrease with decreasing mg.

Maskelynite

The grain shape of interstitial plagioclase (now maskelynite) is controlled by the imposing geometries of pyroxene and olivine. Crystal faces are subhedral and range in size from width 55 μm (30–200 μm) and length 160 μm (80–540 μm). Maskelynite is of labradorite composition, $\text{An}_{61.8-64.6}\text{Ab}_{35.0-37.8}\text{Or}_{0.4-0.5}$ and is relatively homogeneous. A significant amount of Fe (FeO 0.42–0.56 wt%) is detected in EMP analyses.

Minor Minerals

Minor minerals include spinels (low-Ti chromite and Cr-ulvöspinel), ilmenite, merrillite, pyrrhotite, pentlandite, and secondary calcite and iron oxides. Spinel is dispersed throughout the groundmass and occur as inclusions in olivine macrocrysts, forming both single low-Ti chromite and Cr-ulvöspinel grains, and composite grains with low-Ti chromite cores and Cr-ulvöspinel rims. Both individual and composite grains range from 10–160 μm in diameter, and form rounded anhedral grains, or euhedral grains with square-shaped cross sections. Texturally, cores of composite grains are pervaded by short (μm -size), open, irregular fractures that terminate abruptly at fracture-free rims.

Compositionally, spinels associated with olivine macrocrysts and those dispersed in the groundmass are indistinguishable (Fig. 6). Cores of composite spinel grains have low-Ti, with cr-numbers [molar $\text{Cr}/(\text{Cr} + \text{Al}) \times 100$] ranging from 75–84. Rims of Cr-ulvöspinel have cr-numbers in the range of 72–79 and higher Al_2O_3 . Based on

Table 1. Modal composition of SaU 150 compared to data reported for SaU 094/005 and DaG 476.

Meteorite	SaU 150				SaU 094 ^a	DaG 476 ^b	DaG 489 ^c	EET A79001 A ^d
	Point count (n = 4000)							
	Image analysis software							
	Section 1	Section 2	Section 1	Section 2				
Pyroxene (total)	54.6	51.2	54.25	49.81	52.0–58.2	58–60	54	69–73
-clinopyroxene	54.6	51.2	54.30	49.8	52.0–58.2	54.8	50	58.2–71.5
-orthopyroxene	n.p.	n.p.	n.p.	n.p.	n.p.	1.5–3.4	4	3.4–7.2
Olivine	17.2	20.7	17.41	23.13	31.0–22.1	14–17	20	7.0–10
Maskelynite	14.5	14.0	15.46	13.82	8.6–13.7	14–17	17	16–18
Opagues	3.3	3.8	1.57	3.13	1.1–1.1	2.6–3.8	3	2.2–4.0
Merrillite	tr	tr	n.a.	n.a.	tr	tr	1	n.a.
Shock melt	10.2	10.2	11.31	10.18	6.7–4.8	4.0–4.5	4	n.a.
Melt inclusions	0.3	0.2	n.a.	n.a.	0.6, 0.1	n.a.	n.a.	n.a.

^aGnos et al. (2002): commas separate point count determinations on different thin sections of SaU 094.

^bZipfel et al. (2000).

^cFolco et al. (2000).

^dMcSween and Jarosewich (1983).

n.a. = not analyzed; n.p. = mineral/phase is not present in meteorite; tr = trace abundance <0.1 vol%.

stoichiometry and charge-balance recalculations, it was determined that up to 14% of Fe is Fe³⁺. Single grains have similar compositions, with up to 12% Fe as Fe³⁺, and cr 67–76. TiO₂ abundances as high as 20.9 wt% of individual grains are higher than concentrations determined for Ti-rich rims of composite grains (up to ~16 wt% TiO₂). High MgO concentrations (~4–6 wt%) are typical for all spinel analyses.

All phosphate grains are merrillite, and no apatite has been found. Merrillite grains are subhedral to euhedral and tabular, ranging in size from 12–110 μm. Merrillite is relatively homogeneous in composition, with 0.9–1.9 wt% FeO and 3.6–3.8 wt% MgO. Traces of Cl were detected in some analyses.

Ilmenite occurs as 20–30 μm-size anhedral grains associated with chromite in the groundmass. Analyses of ilmenite reveal a homogeneous composition with 0.7 wt% MnO, 2.0–4.2 wt% MgO, and 0.47–0.48 wt% Cr₂O₃. Fe-sulfides are anhedral pyrrhotite (<100 μm) with Fe/S ratios slightly less than 1. Pyrrhotite contains minor amounts of Cr and Co, and grains with pentlandite inclusions (1–3 μm) contain up to 6.7 wt% NiO.

Calcite veins 20–50 μm in thickness crosscut all features (olivine macrocrysts, groundmass minerals), and are typically associated with melt pockets.

Melt Inclusions

Olivine typically contains spinel (1–160 μm), rounded, polyphase silicate melt inclusions (20–300 μm), and massive/blocky silicate inclusions (10–80 μm) (Figs. 6a–c). Pyroxene crystals do not contain melt inclusions. Inclusions are ubiquitous in all studied olivine macrocrysts. The smallest olivine grains in the basaltic groundmass (≤100 μm diameter) typically enclose euhedral spinels, but lack the polyphase silicate melt inclusions.

Olivine-hosted melt inclusions are divided into three distinct types: 1) skeletal clinopyroxene + glass + clinopyroxene rim surrounding the melt inclusion, 2) skeletal and rim clinopyroxene + glass + silica-rich phase, and 3) massive/blocky augite ± silica/aluminium-rich phase.

Clinopyroxene is augite in all melt inclusion types. Skeletal and rim augite in type 1 and type 2 melt inclusions are compositionally indistinguishable, with end member compositions ranging from En_{25.8–41.7}Fs_{13.5–23.6}Wo_{42.1–52.0}. Mg numbers show a significant gap in composition from mg 52–66 and mg 71–76 (Fig. 4). Silica-rich phases are nearly pure silica with 93.8–95.9 wt% SiO₂ and 3.6–5.4 wt% Al₂O₃, yielding Si/Al ratios of 24.2–26.2. These Si-rich phases form rounded blebs. The “glassy” matrix in type 1 and type 2 melt inclusions shows fine dendritic textures in the coarsest melt inclusions (>100 μm) (Fig. 6b). The matrix material is highly variable in composition, yielding silica-rich compositions that are approximately andesitic to dacitic (58.7–69.2 wt% SiO₂, 1.8–6.1 wt% Na₂O + K₂O). Iron sulfide typically occurs as subrounded grains in the melt inclusions.

Type 3 massive/blocky crystals are augite associated with a Si/Al-rich phase, although individual grains of both minerals have been observed. Type 3 inclusions have distinct compositions from type 1 and 2. Augite is more Mg-rich and Ca-poor compared to that of the previously described melt inclusions, with end-member compositions ranging from En_{44.3–48.9}Fs_{15.3–18.4}Wo_{32.0–40.4}, and mg 71–76. Si/Al-rich inclusions of composition 63–78 wt% SiO₂ and 21.2–23.0 wt% Al₂O₃ yield lower Si/Al ratios (3.1–4.5). Regardless of composition, augite in types 1, 2, and 3 melt inclusions contains elevated phosphorus (up to 1.8 wt% P₂O₅), a trend also observed in SaU 005 melt inclusions (Goodrich 2003). Additionally, compositional trends for augite in all melt inclusion types show some interesting

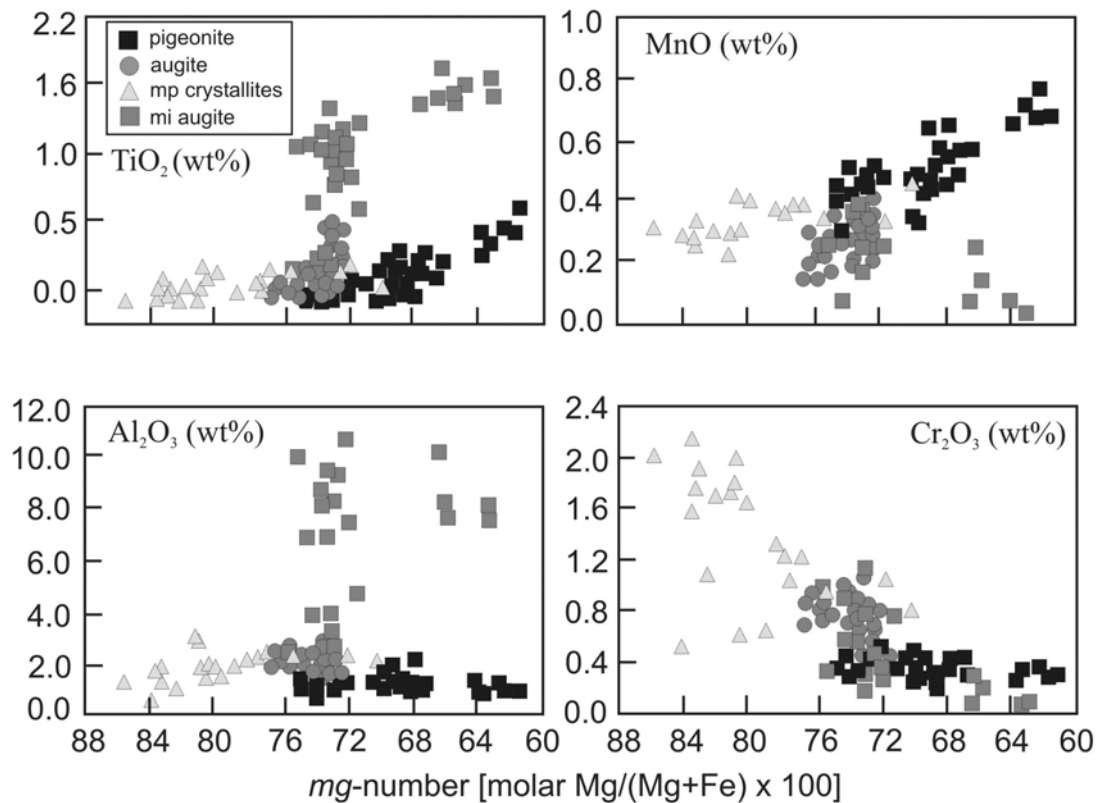


Fig. 4. Variations of TiO_2 , Cr_2O_3 , Al_2O_3 , and MnO relative to mg numbers, in groundmass pyroxenes, and melt pocket pyroxene crystallites from SaU 150. mp = melt pocket, mi = augite occurring as melt inclusions in olivine. See text for discussion.

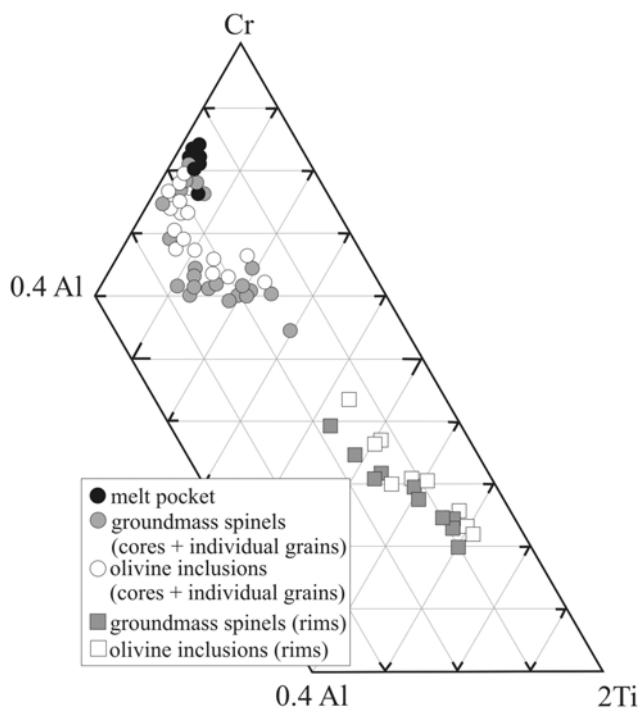


Fig. 5. Compositional data for spinels in the chromite (Cr)-spinel (Al)-ulvöspinel (2Ti) system. All data in mol%.

affinities (Fig. 4). At their highest mg numbers (71–76), TiO_2 and Al_2O_3 show vertical trends. Cr_2O_3 and MnO decrease with decreasing mg.

Skeletal/blocky pyroxene \pm Si/Al-rich phase (glass?) occurs as small, 2–12 μm -size, rounded melt inclusions occurring in individual chromite grains enclosed by olivine, and composite spinel grains dispersed in the groundmass and enclosed by olivine (Fig. 6d). In general, clinopyroxene compositions are similar to massive augite and Si inclusions in olivine, with $\sim\text{En}_{33}\text{Fs}_{27}\text{Wo}_{40}$, with the Si/Al-rich phase having low Si/Al low ratios (~ 4 –5).

Melt Pockets

Melt pockets are manifest as subrounded enclaves of melt material, either as small, 10–100 μm -size pockets, typically developed at olivine-pyroxene grain boundaries, or as larger, mm-size (up to 4.5 mm diameter) irregularly shaped pockets that obscure original grain boundaries (Fig. 2, Fig. 7). Small melt pockets typically have a glassy groundmass with flow-textured schlieren containing abundant spheres/blebs of immiscible sulfides and clasts of locally derived host rock mineral fragments (olivine, pyroxene) (Fig. 7a). Larger mm-size pockets are almost wholly crystalline, containing olivine and pyroxene with dendritic (swallowtail + rod) morphology, idiomorphic chromite and interstitial glass (Figs. 7b–f). They

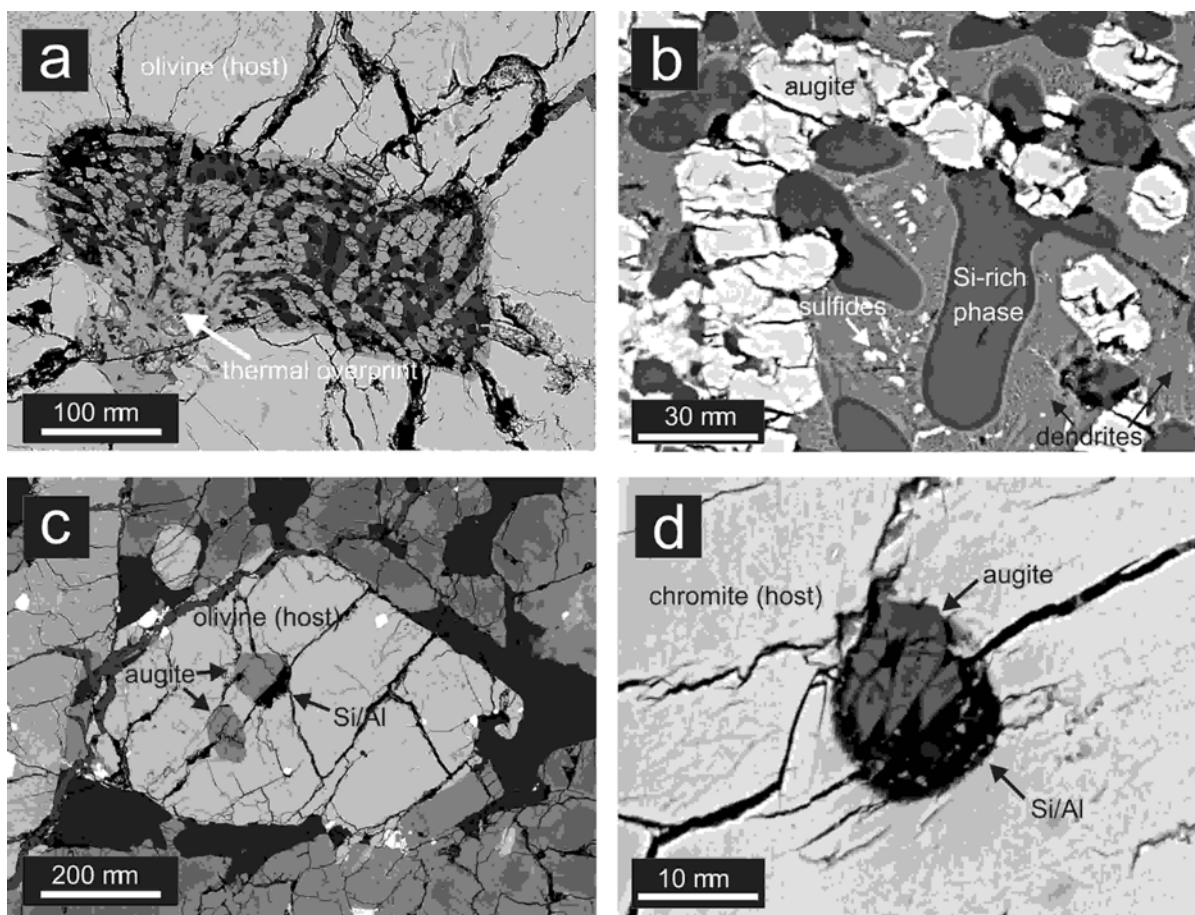


Fig. 6. SEM BSE images of melt inclusions in olivine (a, b, c) and chromite (d). a) A coarse inclusion in olivine with assemblage augite + Si phase + sulfides + glass. Note that the edge of the melt inclusion (indicated by the arrow) shows evidence for later thermal heating and partial melting. b) The “glass” depicted in (a) shows fine dendritic textures at high magnification. c) Massive/blocky augite + Si/Al-rich inclusion in olivine. d) Skeletal augite + Si/Al-rich phase inclusion in chromite.

are also typically highly vesiculated, a feature quantitatively analyzed by X-ray tomographic techniques in SaU 094 by Gnos et al. (2002).

Dendritic olivine crystals, coarse enough for optical characterization, show straight extinction and normal third order interference colors ($\delta = 0.036\text{--}0.045$). Dendrites are colorless in plane light, but, where fine-grained crystals are overlapping in section, they show brown coloration. Dendritic pyroxene is colorless in plane light and shows inclined extinction and first order interference colors ($\delta = 0.08\text{--}0.011$). Sets of parallel rods are observed in thin section, having a common extinction position, suggesting that they belong to the same dendrite (i.e., they are connected out of the plane of the section). This is observed for both olivine and pyroxene dendrites.

Dendritic olivine crystals are strongly zoned; however, their small grain size made quantitative analysis difficult. Olivine cores range from $\text{Fo}_{77.8\text{--}84.2}$ and analyses closer to the rims are less magnesian ($\text{Fo}_{54.9\text{--}69.4}$). X-ray elemental maps of olivine crystallites allow for qualitative characterization of mineral zoning to confirm more ferroan

rim compositions (Fig. 8). Dendritic pyroxene crystals of composition $\text{En}_{63.9\text{--}84.2}\text{Fs}_{14.0\text{--}27.2}\text{Wo}_{1.8\text{--}9.1}$, with mg 70–86 overlap in composition, at their lowest mg values, with those of groundmass pigeonite and augite. Compositional trends are similar, showing increasing TiO_2 , MnO , and Al_2O_3 , and decreasing Cr_2O_3 abundances with decreasing mg, but the compositional range is extended to much higher mg numbers (Fig. 4). No zoning in pyroxene crystallites can be detected by BSE imaging or X-ray mapping. Idiomorphic chromite (1–5 μm), is similar in composition to that of host rock chromite, with cr 81–85 and 2–4% Fe occurring as Fe^{3+} .

BULK COMPOSITION

The bulk rock composition of SaU 150 was calculated using the mineral mode combined with electron microprobe analyses of the mineral phases. Due to the rarity and value of Martian material, this is an ideal method because it is non-destructive. This technique has been successfully applied to other Martian meteorites (e.g., SaU 094 [Gnos et al. 2002] and Yamato-980459 [Greshake et al. 2004]). Results are

Table 2. Bulk composition of SaU 150 compared with those of selected olivine-phyric, basaltic, and lherzolitic shergottites. All data reported as wt% oxides.

Meteorite type	SaU 150 ^a ol-phyric ^g calc	SaU 094 ^b ol-phyric calc	SaU 005 ^c ol-phyric XRF	DaG 476 ^d ol-phyric INAA, XRF	Y-980459 ^e ol-phyric	Shergotty ^f basalt	ALH 77005 ^f lherzolite
SiO ₂	48.24	48.66	47.20	48.91	48.70	51.36	43.08
TiO ₂	0.47	0.26	0.42	0.42	0.54	0.87	0.44
Al ₂ O ₃	5.24	4.12	4.53	4.67	5.27	7.06	2.59
Cr ₂ O ₃	0.61	0.99	0.78	0.83	0.71	0.203	0.963
FeO*	17.21	17.96	18.34	17.17	17.32	19.41	19.95
MnO	0.38	0.50	0.46	0.48	0.52	0.525	0.46
MgO	20.45	22.73	20.49	20.75	19.62	9.28	27.69
CaO	4.58	4.52	5.74	5.84	6.37	10.0	3.35
Na ₂ O	0.70	0.55	0.6	0.55	0.48	1.29	0.44
K ₂ O	0.01	–	0.022	0.041	<0.02	0.189	0.027
P ₂ O ₅	0.06	–	0.31	0.34	0.29	0.80	0.36
NiO	0.02	–	–	–	0.03	–	–
S	0.12	–	–	–	–	0.133	0.060
Total	98.17	100.29	98.892	100.001	99.89		
mg number	68	69	68	68	67	46	71
Fe/Mn	37.9	35.5	40	35.9	33.4	37.1	43.5
Na/Al	0.22	0.22	0.19	0.17	0.13	0.26	0.24

^aThis work. Calculated using mineral modes and average microprobe analyses.

^bGnos et al. (2002). Calculated using mineral modes and average microprobe analyses.

^cDreibus et al. (2000). Calculated using X-ray fluorescence spectroscopy (XRF) for all elements except Na₂O and K₂O, which were analyzed using neutron activation techniques (INAA).

^dZipfel et al. (2000). Calculated bulk composition, combining results of XRF and INAA analyses; CaCO₃ and S-free renormalized.

^eMisawa (2003).

^fCompiled by Banin et al. (1992).

^gOl-phyric: olivine-phyric basalt.

given in Table 2. Major element abundances are similar to those of other olivine-phyric basalts. In particular, the mg number calculated for SaU 150 (68) is identical to those reported for paired olivine-phyric basalt SaU 005/094. Whole rock compositions of selected basaltic and lherzolitic shergottites are shown for comparison (Table 2).

Certain key element ratios are characteristic of all Martian meteorites, reflecting geochemical similarities of element pairs (Wänke and Dreibus 1988). The calculated element ratios for SaU 150 (Fe/Mn = 37.9; Na/Al = 0.22) are well within the range of these characteristic values and match closely those reported for other olivine-phyric basaltic shergottites.

According to the TAS (total alkalis versus silica) classification (Le Bas et al. 1986), SaU 150 is a basalt, consistent with its texture and low modal pyroxene/plagioclase ratio (3.5–3.8). However, a high mg (68) indicates a strong affinity to lherzolitic shergottites. Basaltic shergottites have lower mg values, in the range 23–52 (e.g., Stolper and McSween 1979).

The bulk composition of representative melt pockets are variable from one melt pocket to another. However, some general characteristics arise when CIPW norm calculations are plotted on a ternary diagram (with the major rock-forming minerals at the apices: plagioclase, pyroxene, and olivine)

(Fig. 9). Bulk compositions of small grain boundary hosted melt pockets are highly variable and are not representative of the bulk rock compositions. They are typically mixtures of variable proportions of pyroxene + olivine. Larger, mm-size melt pockets have compositions that are similar to that of the CIPW norm calculated for bulk SaU 150.

SHOCK METAMORPHISM

SaU 150 is an unbrecciated meteorite, recording evidence for a single shock-stage history similar to other Martian meteorites, with the exception of shocked monomict breccias Allan Hills (ALH) 84001 (orthopyroxenite) and Yamato-793605 (lherzolite), which require at least two stages of shock for breccia formation (Mittlefehldt 1994; Ikeda 1997). Shock veins, defined as primarily friction-generated melts, similar to terrestrial micro-pseudotachylytes, have not been identified in the studied sections of SaU 150.

Shock Recorded in the Bulk Rock

Olivine

Olivine macrocrysts show multiple sets of irregular and planar fractures (Figs. 10a and 10b). Planar fractures have spacings of 10–500 μm with up to three intersecting sets,

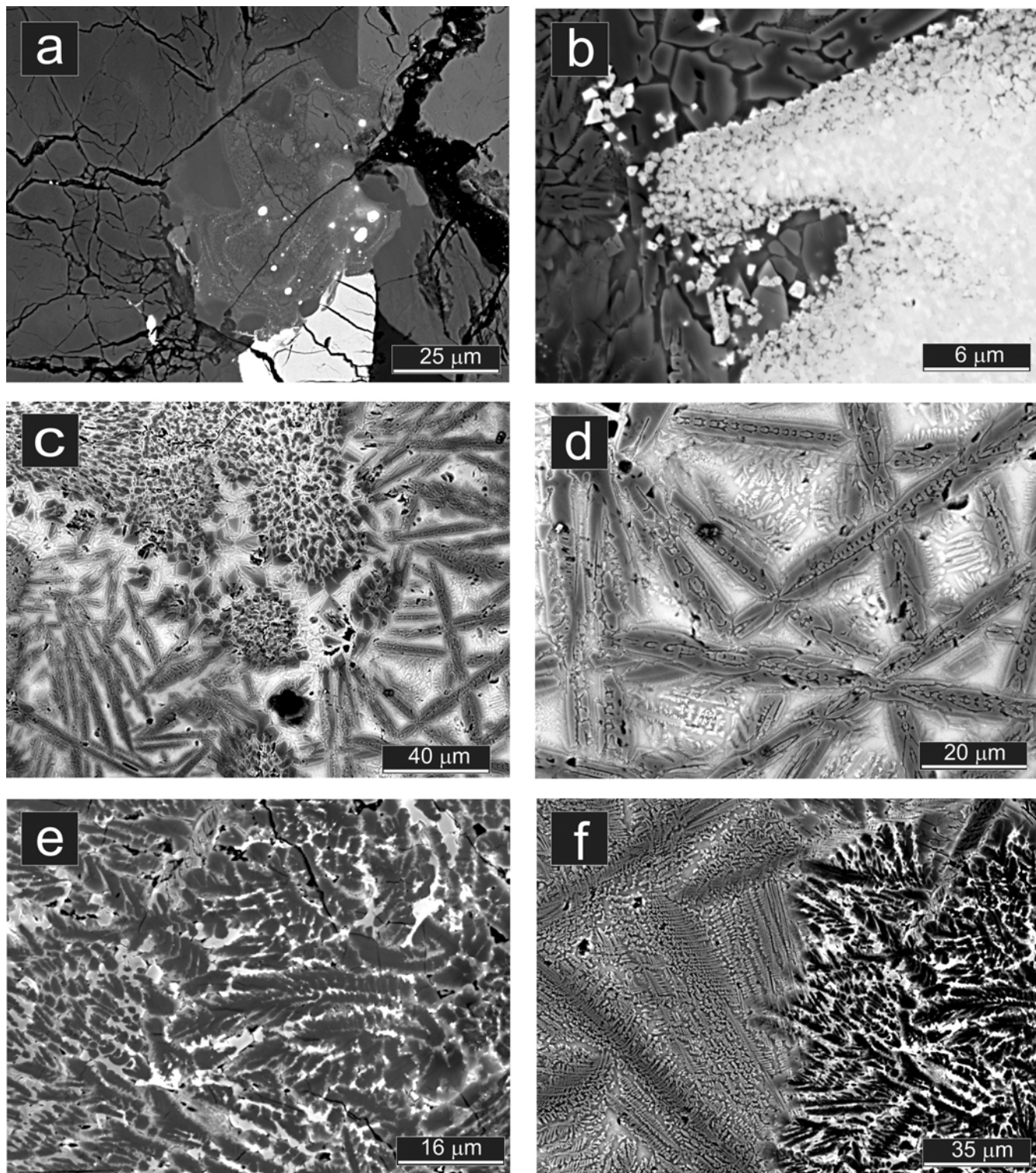


Fig. 7. SEM BSE images of melt pockets in SaU 150. a) Small melt pocket located at the grain margin of host rock olivine and pyroxene. Glassy textures and spheres of immiscible sulfides are visible. "Rafts" of locally derived host rock minerals are embedded within the melt pocket glass. b) Recrystallized idiomorphic chromite in a large melt pocket. c) Texture typical of large mm-size melt pockets having idiomorphic zoned olivine grains and swallowtail morphologies, embedded in a glassy matrix. d) Higher magnification image of swallowtail olivine depicted in (c). e) Dendritic pyroxene morphology in the same melt pocket shown in (a, b, and c). Zoning is not detected. f) Contact between pyroxene and olivine in the same melt pocket.

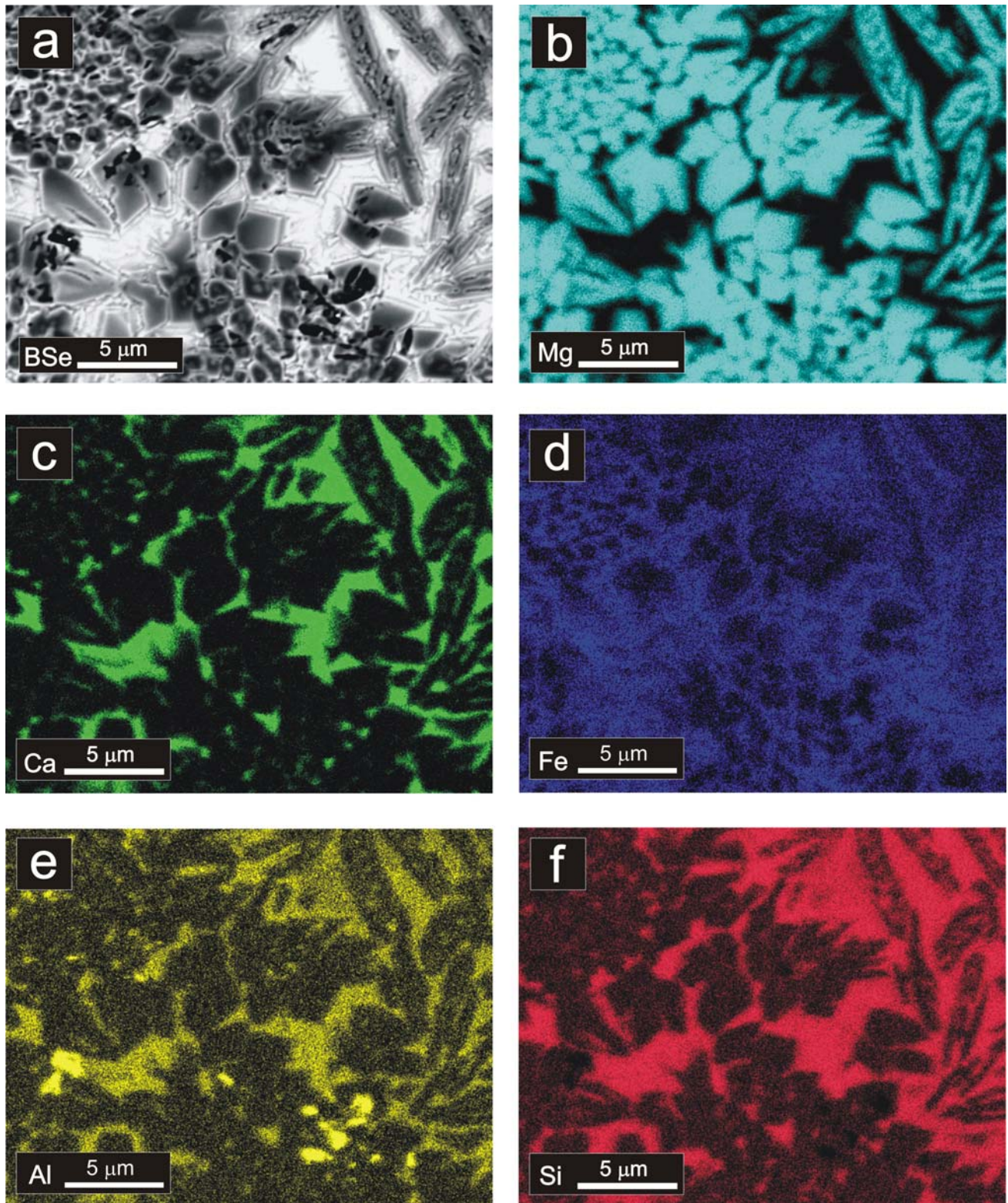


Fig. 8. X-ray elemental mapping of an olivine-rich melt pocket in SaU 150. a) BSE electron image of the area. b) Mg map showing strong Mg enrichment of the cores. c) Ca map showing Ca enrichment in the interstitial glass. d) Fe map revealing pronounced and continuous zoning from a Mg-rich core to Fe-rich rim. e) Al map depicting small grains of an Al-rich phase, and the Al-rich composition of the interstitial glass. f) Si map illustrating Si depletion of olivine crystals with respect to the relatively Si-rich interstitial glass. Al-rich regions correspond to Si-free areas.

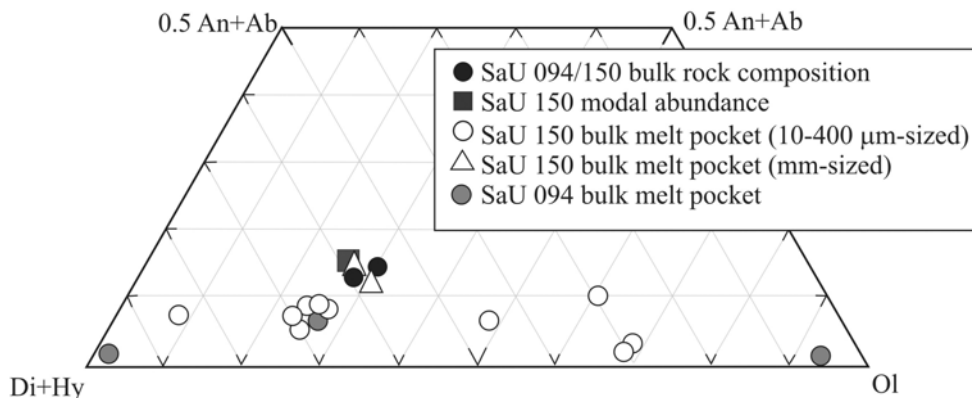


Fig. 9. CIPW norm-corrected data for bulk compositions of melt pockets in SaU 150, compared to the modal abundance of mineral phases (this work), calculated bulk rock composition for SaU 150 (this work), and data from Gnos et al. (2002) for the bulk rock and melt pocket compositions of SaU 094.

although two sets are typical. Macrocrysts with a high density of planar fractures show additional planar elements, observed as short, thin, optical discontinuities with lengths $\sim 10\text{--}30\ \mu\text{m}$. Their spacing is narrower than that of planar fractures ($2\text{--}3\ \mu\text{m}$) and they occur in numerous small blocks, causing strong mosaicism.

Macrocrysts in direct contact with melt pockets show distinct coloration in plane-polarized light (Figs. 10c and 10d). At the contact with small, μm -size glassy melt pockets, olivine shows a darkening in color (dark brown) and planar fractures extend to the olivine-melt contact. Olivine adjacent to large, mm-size hypocrySTALLINE melt pockets is colorless and free of deformation.

Pyroxenes

Pyroxenes are characterized by a high degree of irregular fractures and strong mosaicism. Pigeonite and augite show intense polysynthetic mechanical twinning parallel to (001), observed in prismatic grains. Pyroxene typically contains microfaults that are observed as μm -size displacements of twin lamellae.

Plagioclase

Plagioclase has been completely transformed to maskelynite, with no observable relict birefringence. Maskelynite displays radiating fractures that emanate from their outer margins into neighboring minerals, a feature noted by Chen and El Goresy (2000) for maskelynite in Zagami, DaG 476, and ALH 84001. Normal mineral glasses with plagioclase composition occur as flow-structured and vesiculated glass that is restricted to maskelynite grain boundaries. These are subordinate in abundance to diaplectic glasses.

Opaques

Opaque minerals (spinel, ilmenite, and pyrrhotite) have responded brittly to shock, showing irregular fractures.

DISCUSSION

Crystal Size Distribution

The theory of crystal size distribution (CSD) and its subsequent analysis have been applied in a variety of geological environments to elucidate the crystallization history or formation conditions of terrestrial igneous (e.g., Cashman and Marsh 1988a; Marsh 1998) and metamorphic (e.g., Cashman and Ferry 1988b) rocks. CSD analysis was first applied to pyroxenes in Martian meteorites (nakhlites) by Friedman Lentz et al. (1999) and to shergottites by Lentz and McSween (2000). Subsequently, CSD analysis of olivine macrocrysts has been included in petrographic studies of two olivine-phyric basaltic shergottites: Yamato-980459 (Greshake et al. 2004) and SaU 005 (Goodrich 2003), proving it to be a practical technique for quantitative textural analysis.

CSD Results

Histograms, cumulative histograms and CSD plots for igneous pyroxene and olivine from SaU 150 are given in Fig. 11. Additional information is summarized in Table 3. Following Lentz and McSween (2000), the width of grains was defined as grain size to avoid geometric bias. Grain widths were measured per unit volume on BSE images, following conversion by raising the number measured per unit area to the $3/2$ power (Cashman and Marsh 1988a). Sufficient pyroxene grain numbers were measured (>500) in order to minimize measurement uncertainties. Additionally, since pyroxenes show weak zoning profiles restricted to thin, μm -size rims around grains, core + rim measurements were taken as grain width. Due to the low modal abundance and relative coarse grain size of olivine in the studied sections, a sufficient number of grains (>500) could not be measured. Despite this, some interesting patterns arise from olivine CSD distributions, and these are considered sufficient for interpretation when combined with petrographic observations.

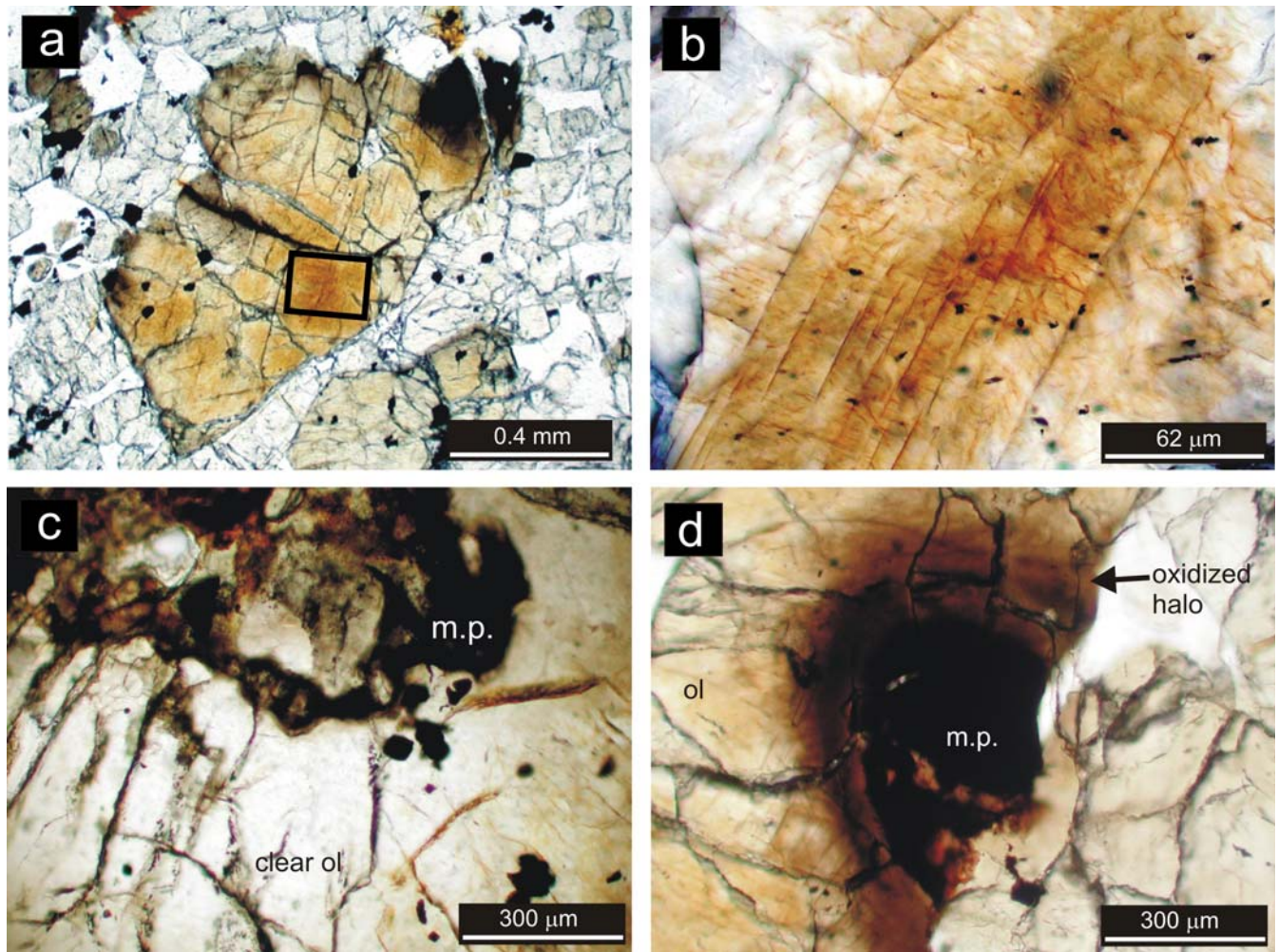


Fig. 10. Shock effects in SaU 150 host rock olivine (plane light images). a) SaU 150 olivine macrocryst. b) An enlargement of the olivine depicted in (a). The area is outlined by the black box. c) Clear, deformation-free olivine adjacent to a large hypocrystalline melt pocket. d) Dark brown oxidized halo in a host rock olivine at the contact with a small, glassy melt pocket. m.p. = melt pocket, ol = olivine.

The shape of the CSD plot of both types of groundmass pyroxene is generally linear with no significant kinks. This curve shape is consistent with a simple crystallization history involving a single growth phase under steady-state conditions of continuous nucleation and growth.

The CSD function for olivine crystals in SaU 150 shows two regimes: a linear trend with negative slope in the size range 0.2 to 1.8 mm, encompassing ~96% of all crystals, and a horizontal trend for crystals >1.8 mm, representing ~4% of all crystals. The first trend indicates olivine crystallization under steady-state conditions of continuous nucleation and growth. The second horizontal trend indicates an overabundance of large crystals. This may result from entrainment of cumulate crystals that grew previously in the same magma, or may invoke more complex scenarios involving addition of xenocrysts or magma mixing. In the latter case, the larger olivine grains would be inherited from one of the magmas (e.g., Marsh 1988; Goodrich 2003).

SaU 150 CSD Plots in Relation to Other Shergottites

Compared to CSD plots of pyroxenes from other olivine-phyric basalts, groundmass pyroxene in SaU 150 yields a CSD curve that is much more shallow than those of DaG 476 and EET A79001 lithology A (Lentz and McSween 2000), indicating a slower cooling time (given a similar growth rate). In contrast, olivine-phyric basalt Yamato-980459 shows a pronounced turnover at the smallest grain sizes, establishing a distinct crystallization history for this meteorite (Greshake et al. 2004). As previously discussed, pyroxenes in Shergotty and Zagami basalts show pronounced kinking in CSD plots (Lentz and McSween 2000). CSD curves for olivine in SaU 150, show similarity with olivine in SaU 005, EET A79001 lithology A and Yamato-980459, having steep negative slopes with horizontal trends at the coarsest grain size. In contrast, the CSD function for olivine crystals in SaU 005, reported by Goodrich (2003), shows a sharp drop off of the curve for crystals <0.24 mm. In terms of CSD theory, this indicates

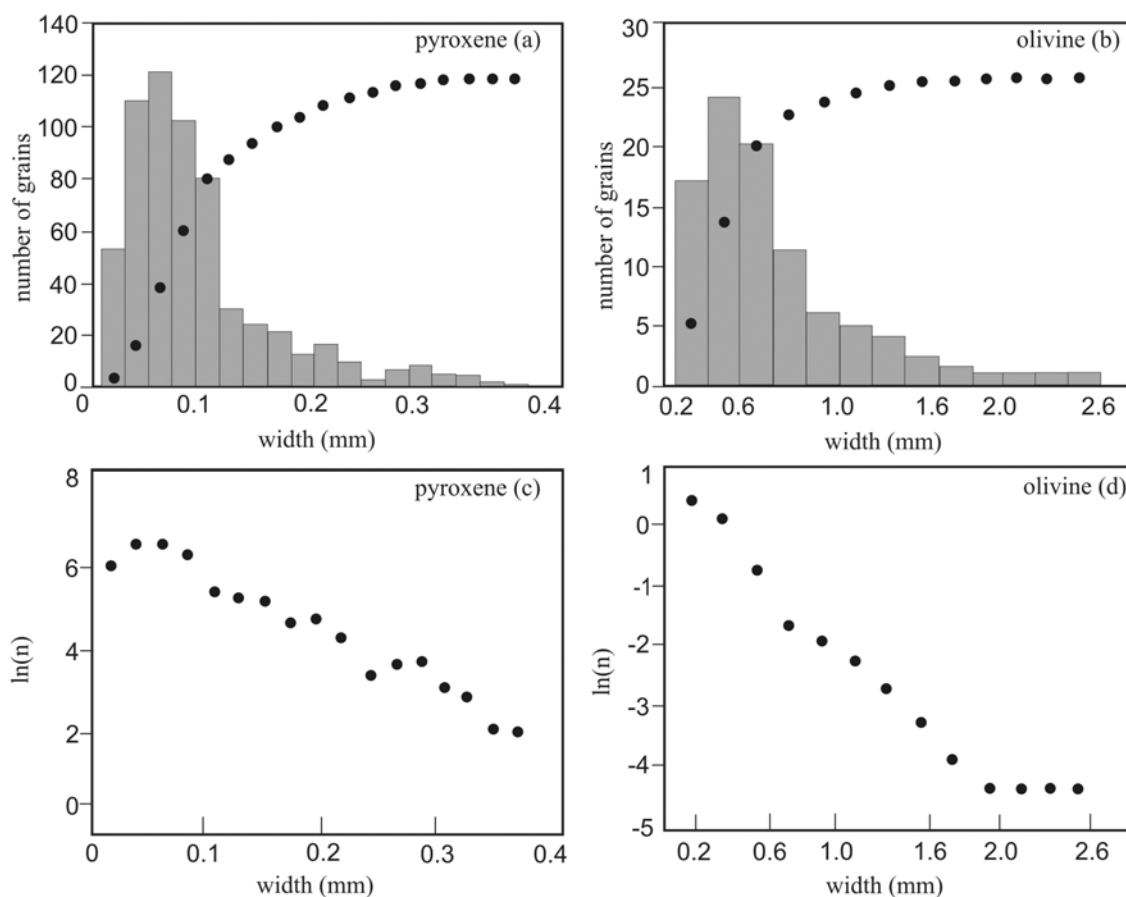


Fig. 11. Pyroxene (core + rim) and olivine in SaU 150. (a, b) Histograms of number of grains versus grain width. The corresponding cumulative histograms (black circles) are superimposed on the histograms. Y-axis scales are only valid for bar histograms. (c, d) Crystal size distribution plots, based on data in (a, b), of $\ln(n)$ versus grain width, where n is dNv^*/dL , Nv^* is the cumulative number of crystals per unit volume ($Nv = [NA]1.5$), and L is grain width.

Table 3. Data from the crystal size distribution study.

Mineral	Avg. width (mm)	St. dev. (mm)	Dom. width (mm)	No grains	Area (mm ²)	Slope ^a	Intercept	R ²	Bin interval (mm)
Pyroxene	0.101	0.064	0.069	553	26.15	-14.53	7.81	0.965	0.001–0.38
Olivine width	0.62	0.62	0.361 ^b	97	50.46	-2.74	1.02	0.963	0.1–2.6
									0.2–1.8

^aBased on weighted least-squares regression for reported bin interval.

^bUsing upper 9 data points.

Dominant width = $G\tau = 1/\text{slope}$.

either a decrease in nucleation rate due to loss of melt at high degrees of crystallization or a cessation of nucleation due to phase equilibria reactions, but with continued growth (annealing of smaller crystals).

Cooling History from Crystal Morphology

Dynamic crystallization experiments simulate the natural cooling histories of magmatic systems. Extensive study of silicate melts has shown that, by comparing the shapes of olivine crystals produced experimentally with those in rocks of similar composition, it is possible to deduce the cooling

rate and the approximate degree of undercooling ($-\Delta T$) at which olivine crystals nucleated and grew (Donaldson 1976; Lofgren 1980; Faure et al. 2003). In particular, there is a consistent pattern of olivine shape variation, with each shape having a specific range of temperature stability. Similar crystallization experiments in lunar basaltic systems have derived pyroxene crystal morphology as a function of cooling rate, but this phase has not been studied as extensively as olivine (Lofgren et al. 1974; Walker et al. 1976). Thus, detailed investigations of olivine and, to a lesser extent, pyroxene morphology in SaU 150 allow constraints to be

placed on the cooling history of the rock. The following discussion follows mainly the approach first applied to Martian meteorite Yamato-980459 by Greshake et al. (2004).

It should be noted that cooling rate parameters are only valid for water-free systems (Donaldson 1976). Furthermore, in cooling experiments, the degree of undercooling can never be precisely determined due to the changing composition of the residual melt during crystallization, resulting in subsequent changes in liquidus temperature. This effect is augmented at rapid cooling rates by the difficulty of dissipating the latent heat of crystallization. Both processes tend to lower $-\Delta T$.

Three distinct types of crystal morphology are present in SaU 150: 1) polyhedral, well-faceted crystals, 2) polyhedral, poorly faceted crystals, and 3) dendritic (quench) morphology. The first two types reflect the igneous cooling history, the latter a thermal event overprinting igneous textures.

Igneous Olivine

Olivine macrocrysts (both smaller unzoned crystals and coarser zoned macrocrysts) are either polyhedral with well-defined faces, or are anhedral in crystal form. The dynamic crystallization experiments of Donaldson (1976) show that runs cooled at a rate of 0.5 °C/hr yield charges containing polyhedral olivine morphologies. This relatively slow cooling regime is consistent with the nearly equant to subequant habits of the observed olivine grains in SaU 150. Crystallization of Fe-free melt compositions shows that the relatively slow cooling rate experiments (1–2 °C/hr) always produce polyhedral crystals, independent of the degree of undercooling (Faure et al. 2003).

Igneous Pyroxene

Pyroxene morphology as a function of cooling rate has been studied in the 1–2000 °C/hr regime (Lofgren et al. 1974). At the slowest cooling rates, <2 °C/hr, pyroxene is generally euhedral, nearly equant, and typically slightly skeletal or blocky.

Melt Pocket Olivine

The morphology of olivine crystals in melt pockets is strikingly different from those of the host rock. They have dendritic (swallowtail and rod) morphology (for terminology, see Faure et al. 2003), indicative of rapid diffusion-controlled growth from a silicate melt (Kirkpatrick 1975). The progression in crystal shapes from polyhedral steady-state growth forms to those of rapid crystal growth (dendrites) represents a changeover from growth that is sensitive to the cooling rate parameter to undercooling-sensitive growth with cooling rate having a minor influence. Dendritic crystals form at temperatures well below the liquidus (large $-\Delta T$), where growth kinetics are not governed by atom selection at the crystal-liquid interface, but by diffusion.

Using an Apollo 12 basalt as starting material, chain olivine (dendritic) forms at 200 °C/hr, lattice (dendritic) at 650 °C/hr (Donaldson 1976). Faure et al. (2003), using Fe-free starting material, showed that dendritic morphologies (swallowtail + rods) crystallize at cooling rates of 225 °C/hr and persist up to 1890 °C/hr. The degree of undercooling is high, $-\Delta T > 70\text{--}356$ °C.

Melt Pocket Pyroxene

The morphology of pyroxene crystallized from shock melts is similar to that of olivine (dendritic). Dynamic crystallization experiments for pyroxene in this regime indicate cooling rates >430 °C/hr (Lofgren et al. 1974).

Fractal Analysis of Melt Pocket Textures

Fractals can be best described as objects that are scale-invariant. In other words, they are made up of self-similar components, appearing the same over a large range in scale (e.g., snowflakes). Fractal analysis allows quantification of natural objects that, at first observation, may appear to be random or chaotic. This is based on the fact that a fractal object is characterized quantitatively by a number, the fractal dimension d_f , that relates the increase in mass M of the object to its characteristic length scale L , $M \sim L^{d_f}$ (Fowler 1990).

Correlation Function

The correlation function technique (Fowler et al. 1989a, 1989b; Fowler 1990, 1995) was used to determine d_f for dendritic olivine and pyroxene crystals in large, mm-size, hypocrySTALLINE melt pockets within SaU 150 and crystallites in a similar melt pocket in DaG 476 (Fig. 13). The goal of this study is to examine the mineral crystallinity (i.e., the perimeter) in order to quantify the melt pocket textures and to compare melt pocket textures between paired meteorites that have, presumably, experienced a similar shock history (SaU shergottites and DaG shergottites).

In practice, BSE images of dendritic (olivine and pyroxene) crystals in the melt pockets are converted to binary maps. All pixels belonging to the texture are black and all non-textured pixels are white. BSE images, taken from roughly two orders of magnitude in scale, ensure that information gathered at any given scale is not biased (Fowler 1995). Fractal analysis is performed by choosing a black/textured pixel as the origin of a series of concentric shells, constructed with increasing radii r (in pixels). Any pixel in the radius circle that is also black counts towards the correlation. The correlation function, $C(r)$, is calculated by dividing the total number of black pixels by the total number of pixels (black + white). This gives the probability that a pixel separated from the local origin by distance, r , is part of the texture. This function has been shown to scale in the same way as the density of pixels in a two dimensional fractal object (Fowler et al. 1989a), i.e., the number of pixels that

belongs to the texture is not proportional to the square of r , but to the power d_f , $C(r) = r^{d_f-2}$. Thus, a quantitative value of d_f can be obtained from a double logarithmic density-density plot of $\log C(r)$ versus $\log r$.

Before plotting, the correlation function is scaled to an integer in the range of 0 to 255. Typically, the raw correlation number would be between 0 and 1 (0 = all white and 1 = all black), however, this program generates a new map as an 8-bit grayscale image. Normalized correlation values, $nC(r)$, thus directly correspond to the gray level in the final image map (Figs. 12a–d). This process of picking a texture pixel as the original of a series of subshells is repeated for all black pixels. The data collected for each value of r are then averaged and plotted on a graph of $\log nC(r)$ versus $\log r$. If the analyzed texture is fractal, a straight line relationship is obtained. For comparison, an item of constant mass distribution, such as a euhedral phenocryst, would have $m = 0$ hence $d_f = 2$, that of a compact, constant density object (Mandelbrot 1983).

Correlation Function Results

Normalized correlation maps and corresponding density-density plots for olivine and pyroxene dendrites are shown in Figs. 12e–h. In total, 14 crystals were analyzed (4 olivine crystals/meteorite, 3 pyroxene crystals/meteorite) over a range of scales. All analyzed minerals fall on a straight line with negative slope, confirming their fractal nature. SaU 150 olivine dendrites fall on a straight line of slope -0.11 to -0.20 , corresponding to $d_f = 1.80$ – 1.89 . Olivine dendrites in DaG 476 melt pockets show a similar range with slope -0.10 to -0.17 , and $d_f = 1.82$ – 1.90 . Similar to the fractal analysis of olivine, pyroxene dendrites in SaU melt pockets fall on a straight line with slope -0.05 to -0.11 , yielding $d_f = 1.89$ – 1.95 . The slope of DaG 476 melt pocket pyroxene dendrites range from -0.10 to -0.18 , with corresponding $d_f = 1.82$ – 1.90 .

Pairing Between SaU 150 and Other Olivine-Phyric Shergottites

Olivine-phyric shergottites are a newly emerging, distinct type of Martian meteorite, currently represented by eight meteorites: DaG 476/489/735/670/876/975/1037, Dhofar 019, EET A79001 lithology A, NWA 1068/1110/1075/2373, NWA 1195, NWA 2046, SaU 005/051/094/060/090/120/150/125/130, and Yamato-908459. The DaG (7 paired meteorites) and SaU (10 paired meteorites) are hereafter referred to as the DaG shergottites and SaU shergottites, except when referring to individual meteorites from specific citations.

Pairing between SaU 150 and SaU 005/094 is supported by 1) texture, 2) major mineral chemistry, 3) flat compositional profiles of constituent host rock minerals, 4) melt inclusion composition and occurrence, 5) mineral mode, in particular the presence of olivine and chromite macrocrysts, high pyroxene/plagioclase ratios and low augite

contents, 6) bulk rock properties, most importantly a high bulk mg number, and Fe/Mn and Na/Al ratios, 7) absence of orthopyroxene macrocrysts, 8) similar olivine CSD functions, 9) overlapping CRE ages, and 10) a close spatial relationship between meteorite finds, forming a strewn field ($\sim 2 \times 3.6$ km) in the Sayh al Uhaymir region of Oman.

Minor discrepancies between SaU 150 and SaU 005 (Goodrich 2003) include 1) the gap in augite composition between mg 73–78, as reported for SaU 005, is not observed in SaU 150 but is continuous through mg 72–76, showing a significant gap from mg 66–72, 2) the CSD function for olivine, although similar, does not show a sharp drop off of the curve for crystals <0.25 mm, as observed for SaU 005, 3) the most magnesian core compositions for SaU 005 ($Fo_{>70}$ up to Fo_{74}), are higher than those found in SaU 150 (max Fo_{70}), despite extensive analysis of core compositions; and 4) occasionally, olivine macrocrysts in SaU 150 have their most Mg-rich compositions at the rim. Discrepancies in CSD function plots are attributed to the small population measured for CSD plots, owing to the coarse grain size of olivine macrocrysts, such that a statistically representative population could not be measured. Additionally, Goodrich (2003) used CSD functions based on the measurement of the maximum length of olivine crystals, which may have introduced a geometric bias. Minor variation in mineral composition is probably the result of sectioning and sample heterogeneity. Also, since large olivine macrocrysts yielding the highest forsterite component comprise only a few vol% abundance, it is not surprising that the most Mg-rich compositions were not sectioned.

SaU 005 is strongly LREE-depleted (Dreibus et al. 2000), belonging to a group of Martian meteorites that are derived from a reservoir or reservoirs formed early in Martian differentiation history, indicated by high initial ϵ_{Nd}^{143} values and ^{142}Nd anomalies (e.g., Jagoutz et al. 2001; Borg et al. 2001). Olivine-phyric shergottites DaG 476 and Dhofar 019, in addition to basaltic shergottite QUE 94201, share the same characteristics. Detailed petrographic and mineralogical variations, coupled with the large distance between the two strewn fields, indicate that, although closely related, DaG-shergottites are not paired with the SaU-shergottite finds (Dreibus et al. 2000; Zipfel et al. 2000). Nishiizumi et al. (1999) presented a ^{14}C - ^{10}Be terrestrial age of ~ 85 ka for the DaG-shergottites, while for SaU 005, a terrestrial age of ~ 13 ka is reported (Nishiizumi et al. 2001), confirming two distinct terrestrial residence times, and hence two distinct fall events.

The Nature of Olivine Macrocrysts

The conclusion by Goodrich (2003) that a small fraction of material in olivine-phyric shergottites SaU 005 and EET A79001 lithology A is xenocrystic is supported by the results of this study for SaU 150. Lines of evidence in favor of this

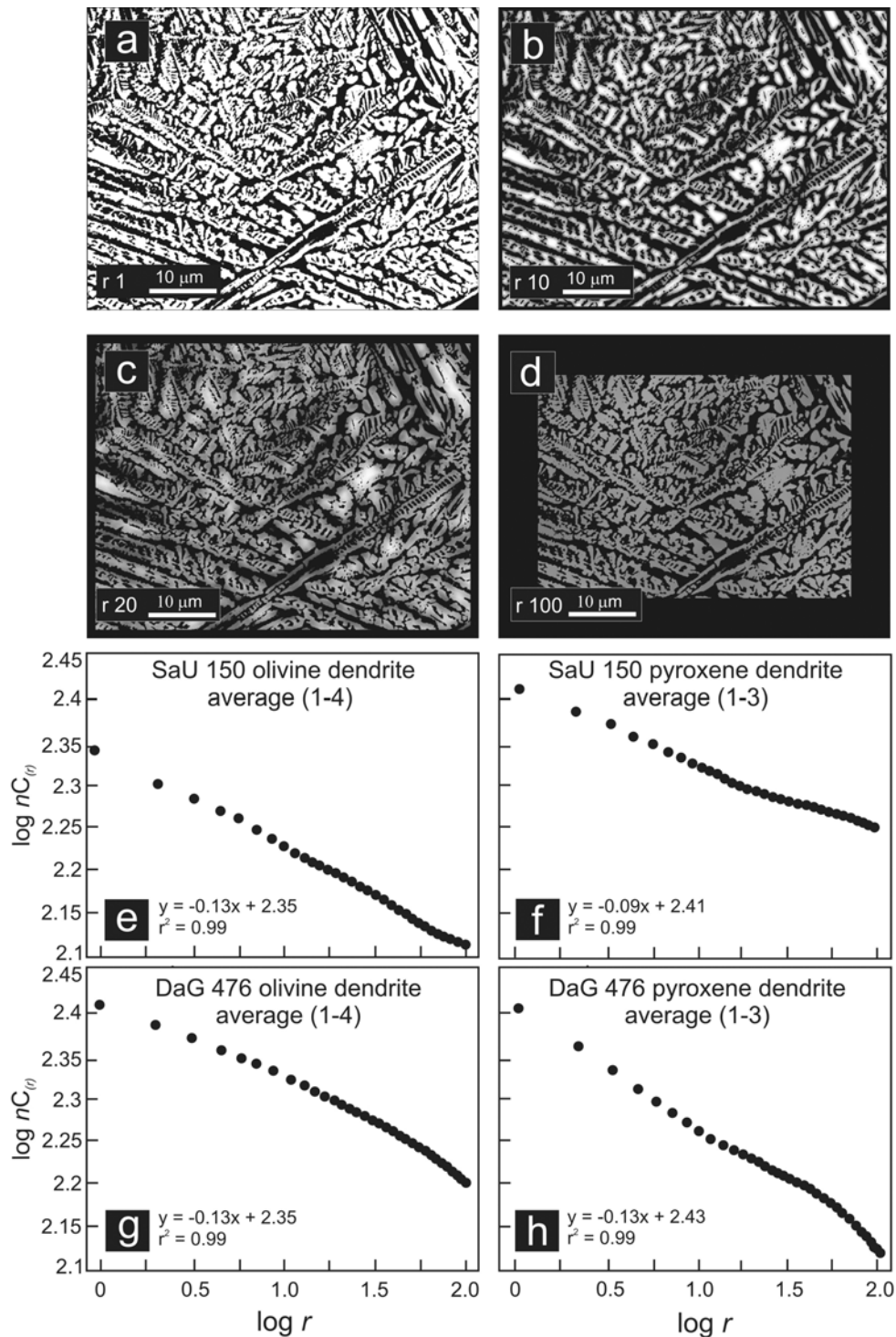


Fig. 12. Fractal analysis of dendritic olivine and pyroxene crystallites in SaU 150 melt pockets compared with those observed in DaG 476 melt pockets. (a, b, c, and d) 8-bit grayscale maps of analyzed olivine textures in SaU 150 melt pocket for radii (in pixels) 1, 10, 20, and 100, respectively. The gray level of each pixel corresponds to the calculated normalized correlation function, $nC_{(r)}$, for that pixel, such that pixels that are black have a low correlation value, white pixels are highly correlated, and points in between are gray. The black frames bordering maps are areas that cannot be calculated because they are too close to the edge of the map for the given radius. (e–h) Double logarithmic density-density correlation plots calculated for r 1–100 in steps of 2 ($nC_{(r)} = (\text{number black pixels}/\text{total pixels}) \times 255$). (e) SaU olivine $d_f = 2 + \text{slope} = 1.87 \pm 0.01$. Total pixels counted range from 412,793 to 242,113 with increasing r . (f) SaU pyroxene, yield $d_f = 1.91 \pm 0.01$. Total pixels counted range from 500,943 to 353,707 with increasing r . (g) DaG olivine, $d_f = 1.86 \pm 0.01$ obtained from a total pixel count of 375,958 to 231,430 with increasing r . (h) DaG pyroxene, $d_f = 1.86 \pm 0.01$. Total pixels counted range from 379,885 to 216,997 with increasing r .

interpretation include: 1) a pronounced turnover at the coarsest olivine grain sizes of CSD plots, which indicates their addition as phenocrysts or xenocrysts, 2) embayment of groundmass material in olivine of the coarsest grain size, suggesting reaction with the groundmass, 3) cores of composite spinel grains are pervaded by fractures that do not extend to ulvöspinel rims, suggesting a previous history of physical stress for the cores prior to rim overgrowth, 4) a small fraction of olivine macrocrysts have Mg-rich compositions at the rim, interpreted to result from fragmentation and disruption of olivine cores during transport, and 5) following calculations by Mikouchi et al. (2001) for DaG 476, a melt having the bulk composition of SaU 150 (mg 68) would be in equilibrium with olivine of Fo_{86} . This is much more magnesian than even the most Mg-rich core compositions observed (Fo_{70}). Although this does not conclusively point to a xenocrystic origin, it is possible to assume that olivine grains are either xenocrysts or phenocrysts that crystallized after the melt previously crystallized more magnesian phases (Mikouchi et al. 2001). As pointed out by Goodrich (2003), the conclusion that a small fraction of material is xenocrystic or xenolithic implies loss of fractionated liquids during the late stages of crystallization.

Shock Metamorphic Effects

Equilibration Shock Pressure

The equilibration or peak shock pressure (for terminology, see Stöffler et al. 1991), as recorded in the bulk rock, can be estimated by comparing observed shock effects in meteorites with those accurately calibrated from a comprehensive set of shock recovery experiments on single crystals, terrestrial rocks, and chondrites (e.g., Schmitt 2000). That plagioclase has been completely transformed to maskelynite, with no relict birefringence, yields a lower pressure limit of 33.4 GPa (Schaal and Hörz 1977; Stöffler et al. 1991). Based on the overall shock effects in olivine and pyroxene (abundance of planar and irregular fractures + mosaicism), coupled with the presence of maskelynite, equilibration shock pressures can be bracketed from ~33–45 GPa. This lies within the supposed ‘launch window’ for Martian meteorites, which spans, at the lower limit, ~5 GPa (for nakhlites Lafayette and Yamato-000593) to 45 GPa (for basaltic shergottites Los Angeles, QUE 94201, and lherzolic shergottites ALH 77005 and LEW 88516) (Fritz et al. 2002, 2003). In particular, this corresponds to high equilibration shock pressures quantitatively determined for DaG 476 (42.9 ± 2.0 GPa), and SaU 005 (42 ± 2 GPa), based on high precision refractive index measurements of plagioclase and on the experimental calibration of the refractive index by shock recovery experiments (Fritz et al. 2002, 2003). This further supports pairing between SaU 150 and SaU 005, with strong affinities to DaG-shergottites. A peak shock pressure

in excess of 45 GPa reported for SaU 094 by Gnos et al. (2002) is regarded as an overestimate, because, at these pressures, plagioclase would have been completely shock fused (Stöffler 2000).

Localized Melt Pockets

Localized melt pockets are interpreted to be shock-produced melts, due to 1) their crosscutting relationships with igneous textures, 2) gradational contacts with host rock minerals, and 3) annealing of mechanical shock defects in olivine adjacent to the melt pockets. This is manifest as a zone of clear olivine, free of planar and irregular fractures, rather than possessing a distinct brown coloration arising from shock oxidation (Ostertag et al. 1984).

Zoning of olivine crystallites, coupled with the observation that textures vary between melt pockets of different sizes, and from individual melt pocket margins to cores, indicates that they formed by diffusion-controlled growth from a silicate melt, rather than by the devitrification of glasses. Based on chemical composition and optical properties, pyroxene is interpreted to be monoclinic, and olivine as orthorhombic. No high-pressure phases were identified at this scale (i.e., ringwoodite or majorite, both of which have distinct coloration and are isotropic). Additionally, chromite morphology and grain size indicates complete melting and recrystallization of primary igneous chromite.

Crystals characteristic of diffusion-controlled growth have been previously reported in a variety of rock types and settings including pillow basalts (Bryan 1972; Fowler et al. 1989a), comb-layered rocks (Lofgren and Donaldson 1975), dykes (Ohnenstetter and Brown 1992), chondrules (Lofgren 1989), impact-related spherules (Kyte and Bostwick 1995), pseudotachylyte (Maddock 1983), and komatiites (Donaldson 1982). Recently, these environments have been extended to include Martian meteorites, in the form of quench textures in thin lava flows (Yamato-980459; Greshake et al. 2004), and shock-generated melts (this study), both of which are characterized by disequilibrium crystals of dendritic morphology. Textures observed in hypocrySTALLINE shock melts are characteristic of disequilibrium crystals formed at large degrees of undercooling, and their scale-invariant properties allow determination of their fractal dimensions. The fractal dimension provides a more quantitative index of melt pocket textures, and provides a novel approach for comparison between melt pocket crystallites within a given meteorite or between meteorites. Any given fractal dimension is unique to a particular crystal shape. Overlapping d_f of olivine and pyroxene dendrites in SaU 150 and DaG 476 melt pockets is interpreted to indicate crystallization under similar cooling conditions after shock pressure release. Additionally, high d_f values (>1.8), confirm their growth under far-from-equilibrium conditions, i.e., at large degrees of undercooling

(see Fowler 1995 for discussion). A developmental model of forsterite morphology (Faure et al. 2003) shows that these crystals are formed by repetition in the third dimension of the same hopper unit, in further support of their fractal nature.

Formation of Melt Pockets

Study of melt pocket textures in SaU 150 infers crystallization under conditions of ambient pressure at high degrees of undercooling, forming dendritic olivine and pyroxene. Thus, post-shock temperatures must have been high enough to maintain fluid conditions after pressure release. These conditions do not favor the formation and preservation of high pressure polymorphs, which is consistent with the observed melt pocket mineralogy. The mechanism for generating focused shock melting in heterogeneous target rocks remains largely unresolved. There is general agreement that shock impedance (shock wave velocity \times mineral density) contrasts are a major factor in forming these melts. These conditions may be accentuated by highly incompressible minerals (olivine, chromite), or the presence of pore space. The existence of primary pore space in generating high post-shock temperature excursions has been proposed by Greshake and Stöffler (2000) for melt pockets in DaG 476, and by Wiens and Pepin (1986) and Bogard et al. (1986, 1989) to explain the high emplacement efficiencies of a Martian atmospheric component in shock glasses found in EET A79001. Shock recovery experiments demonstrate that hypervelocity impact provides a viable mechanism for emplacement of ambient gases without elemental or isotopic fractionation.

The results of this study favor in situ formation of melt pockets based on 1) gradational contacts between melt pockets and host rock minerals, 2) the observation that bulk melt pocket compositions are heterogeneous, reflecting the local surrounding mineralogy, and 3) as melt pocket size increases the composition approaches that of the bulk rock, which would be expected if they formed by in situ melting, incorporating progressively larger volumes of the host rock mineralogy. Injected shock melt would not be expected to reflect the mineralogy of the host rock and would be expected to have an intrusive contact relationship with the host rock, containing abundant clasts of host rock material. Although these findings do not point directly to a void collapse scenario, they are consistent with the textures expected from such a formation mechanism. Calcite, infilling veins, and cavities associated with these shock melt pockets are interpreted to be terrestrial in origin due to their crosscutting nature.

CONCLUSION

From an investigation of crystal morphology, mineralogy and rock texture, the following crystallization history is proposed for SaU 150:

1. A steady-state crystal growth regime wherein the polyhedral olivine morphology and prismatic pyroxene grains are cooled at rates 0.5–2 °C/hr in a sub-surface magma chamber.
2. Eruption as a relatively thick lava flow (or a shallow intrusion), entraining a small fraction of xenocrystic olivine, and giving rise to a preferred alignment of entrained prismatic pyroxene and olivine grains, with relatively slow cooling allowing near chemical equilibration of host rock minerals.
3. Shock-induced spallation from a near-surface environment at peak shock pressure of ~33–45 GPa. Post-shock heat gave rise to localized melt pockets that crosscut igneous textures and have annealed mechanical shock defects in neighbouring host rock olivine. Some of the larger volume melts remained in the molten state after pressure release to crystallize dendritic olivine and pyroxene with fractal dimensions 1.80–1.89 and 1.89–1.95, respectively, at large degrees of undercooling ($-\Delta T > 70$ –365 °C).
4. Residence time in a terrestrial hot desert environment forming calcite in veins and cavities.

SaU 150 is an olivine-phyric basalt paired with the SaU 005/094 find. A single-stage shock history for SaU 150 is consistent with its origin as a thick volcanic flow or hypabyssal intrusion and subsequent launch by spallation of near-surface material during a recent impact cratering event. The recognition of olivine-phyric shergottites as a new and distinct Martian magma type requires further expansion of the traditional SNC classification scheme in order to reflect the petrological diversity of the current Martian meteorite suite.

Acknowledgments—This work has been funded by NSERC and the Canadian Space Agency through grants to ELW, and NSERC grants to JGS. Thanks to Douglas Hall for EMP assistance and Steven Cogswell for writing computer code, both located at the Microscopy and Microanalysis Facility, UNB. Thanks also to Angsar Greshake and an anonymous reviewer whose comments improved an earlier draft of this work. This is Planetary and Space Science Centre Contribution 43.

Editorial Handling—Dr. Edward Scott

REFERENCES

- Banin A., Clark B., and Wänke H. 1992. Surface chemistry and mineralogy. In *Mars*, edited by Kiefer H. H., Jakosky B. M., Snyder C. W., and Mathews M. S. Tucson: The University of Arizona Press. pp. 594–625.
- Barrat J. A., Jambon A., Bohn M., Gillet P., Sautter V., Göpel C., Lesourd M., and Keller F. 2002. Petrology and chemistry of the picritic shergottite Northwest Africa 1068 (NWA 1068). *Geochimica et Cosmochimica Acta* 66:3505–3518.

- Bartoschewitz R. and Appel P. 2003. Sayh al Uhaymir 150—A further fragment of the SaU-shergottite shower (abstract). *Meteoritics & Planetary Science* 38:A38.
- Bogard D. D., Hörz F., and Johnson P. H. 1986. Shock-implanted noble gases: An experimental study with implications for the origin of martian gases in shergottite meteorites. *Journal of Geophysical Research* 91:E99–E114.
- Bogard D. D., Hörz F., and Johnson P. H. 1989. Shock-implanted noble gases II: Additional experimental studies and recognition in naturally shocked terrestrial materials. *Meteoritics* 24:113–123.
- Bogard D. D. and Garrison D. H. 1999. ^{39}Ar - ^{40}Ar “ages” and trapped argon in martian shergottites, Chassigny, and Allan Hills 84001. *Meteoritics & Planetary Science* 34:451–473.
- Borg L. E., Nyquist L. E., Reese Y., Weismann C.-Y., Ivanova M., Nazarov M. A., and Taylor L. A. 2001. The age of Dhofar 019 and its relationship to the other martian meteorites (abstract #1144). 32nd Lunar and Planetary Science Conference. CD-ROM.
- Bryan W. B. 1972. Morphology of quench crystals in submarine basalts. *Journal of Geophysical Research* 77:5812–5819.
- Cashman K. V. and Marsh B. D. 1988. Crystal size distribution (CSD) in rocks and the kinetics and dynamics of crystallization. II: Makaopuhi lava lake. *Contributions to Mineralogy and Petrology* 99:292–305.
- Cashman K. V. and Ferry J. M. 1988. Crystal size distribution (CSD) in rocks and the kinetics and dynamics of crystallization. 3: Metamorphic crystallization. *Contributions to Mineralogy and Petrology* 99:401–415.
- Chen M. and El Goresy A. 2000. The nature of maskelynite in shocked meteorites: Not a diaplectic glass but a glass quenched from shock-induced dense melt at high pressures. *Earth and Planetary Science Letters* 179:489–802.
- Clayton R. N. and Mayeda T. K. 1996. Oxygen isotope studies of achondrites. *Geochimica et Cosmochimica Acta* 63:1459–1470.
- Crozaz G. and Wahwa M. 2001. The terrestrial alteration of Saharan shergottites Dar al Gani 476 and 189: A case study of weathering in a hot desert environment. *Geochimica et Cosmochimica Acta* 65:971–977.
- Donaldson C. H. 1976. An experimental investigation of olivine morphology. *Contributions to Mineralogy and Petrology* 57:187–213.
- Donaldson C. H. 1982. Spinifex-textures komatiites: A review of textures, compositions and layering. In *Komatiites*, edited by Arndt N. T. and Nesbit E. G. London: Allen and Unwin. pp. 213–244.
- Dreibus G., Spettel B., Haubold R., Jochum K. P., Palme H., Wolf D., and Zipfel J. 2000. Chemistry of a new shergottite: Sayh al Uhaymir 005 (abstract). *Meteoritics & Planetary Science* 35:A49.
- Faure F., Trolliard G., Nicollet C., and Montel J.-M. 2003. A developmental model of olivine morphology as a function of the cooling rate and the degree of undercooling. *Contributions to Mineralogy and Petrology* 145:251–263.
- Folco L., Franchi I. A., D’Orazio M., Rocchi S. M., and Schultz L. 2000. A new martian meteorite from the Sahara: The shergottite Dar al Gani 489. *Meteoritics & Planetary Science* 35:827–839.
- Fowler A. D., Stanley H. E., and Daccord G. 1989a. Disequilibrium silicate mineral textures: Fractal and non-fractal features. *Nature* 341:134–138.
- Fowler A. D., Roach D., and Thériault R. 1989b. Statistical and fractal models of nonequilibrium mineral growth. In *Statistical applications in the earth sciences*, edited by Agterberg F. P. and Bonham-Carter G. F. Ottawa: Geological Survey of Canada. pp. 249–254.
- Fowler A. D. 1990. Self-organized mineral textures of igneous rocks: The fractal approach. *Earth Science Reviews* 29:47–55.
- Fowler A. D. 1995. Mineral crystallinity in igneous rocks: Fractal method. In *Fractals in the earth sciences*, edited by Barton C. C. and La Point P. R. New York: Plenum Press. pp. 237–249.
- Franchi I. A., Wright I. P., Sexton A. S., and Pillinger C. T. 1999. The oxygen isotopic composition of Earth and Mars. *Meteoritics & Planetary Science* 34:657–661.
- Friedman Lentz R. C., Taylor G. C., and Treiman A. H. 1999. Formation of a martian pyroxenite: A comparative study of the nakhlite meteorites and Theo’s flow. *Meteoritics & Planetary Science* 34:919–932.
- Fritz J., Greshake A., Hecht L., and Stöffler D. 2002. Shock metamorphism of martian meteorites: New data from quantitative shock barometry (abstract #1504). 33rd Lunar and Planetary Science Conference. CD-ROM.
- Fritz J., Greshake A., and Stöffler D. 2003. Launch conditions for martian meteorites: Plagioclase as a shock pressure barometer (abstract #1335). 34th Lunar and Planetary Science Conference. CD-ROM.
- Gnos E., Hofmann B., Franchi I. A., Al-Kathiri A., Hauser M., and Moser L. 2002. Sayh al Uhaymir 094: A new martian meteorite from the Oman desert. *Meteoritics & Planetary Science* 37:835–854.
- Goodrich C. A. 2003. Petrogenesis of olivine-phyric shergottites Sayh al Uhaymir 005 and Elephant Moraine A79001 lithology A. *Geochimica et Cosmochimica Acta* 67:373–377.
- Greshake A. and Stöffler D. 2000. Shock-related melting phenomena in the SNC meteorite Dar al Gani 476 (abstract #1043). 31st Lunar and Planetary Science Conference. CD-ROM.
- Greshake A., Fritz J., and Stöffler D. 2004. Petrology and shock metamorphism of the olivine-phyric shergottites Yamato-980459: Evidence for a two stage cooling and a single stage ejection history. *Geochimica et Cosmochimica Acta* 68:2359–2377.
- Grossman J. N. 2000. The Meteoritical Bulletin, No. 84. *Meteoritics & Planetary Science* 35:A199–A225.
- Grossman J. N. and Zipfel J. 2001. The Meteoritical Bulletin, No. 85. *Meteoritics & Planetary Science* 36:A293–A322.
- Ikeda Y. 1997. Petrology and mineralogy of the Y-793605 martian meteorite. *Antarctic Meteorite Research* 10:13–40.
- Irving A. J., Bunch T. E., Kuehner M., and Wittke J. H. 2004. Petrology of primitive olivine-orthopyroxene-phyric shergottites NWA 2046 and NWA 1195: Analogies with terrestrial boninites and implications for partial melting of hydrous martian mantle (abstract #1722). 33rd Lunar and Planetary Science Conference. CD-ROM.
- Jagoutz E., Jotter T., and Dreibus G. 2000. Evolution of six SNC meteorite with anomalous neodymium-143. (abstract). *Meteoritics & Planetary Science* 35:A83–A84.
- Kirkpatrick R. J. 1975. Crystal growth from the melt: A review. *American Mineralogist* 60:798–814.
- Kyte F. T. and Bostwick J. T. 1995. Magnesioferrite spinel in Cretaceous/Tertiary boundary sediments of the Pacific basin: Remnants of hot, early ejecta from the Chicxulub impact? *Earth and Planetary Science Letters* 176:259–265.
- Le Bas M. J., Le Maitre R. W., Streckeisen A., and Zanettin B. 1986. A chemical classification of volcanic rocks based on the total alkali-silica diagram. *Journal of Petrology* 27:745–750.
- Lentz R. C. and McSween H. Y., Jr. 2000. Crystallization of the basaltic shergottites: Insights from crystal size distribution (CSD) analysis of pyroxenes. *Meteoritics & Planetary Science* 35:919–927.
- Lofgren G., Donaldson C. H., Williams R. J., Mullins O., Jr., and Usselman M. 1974. Experimentally reproduced textures and

- minerals chemistry of Apollo 15 quartz normative basalts. Proceedings, 5th Lunar Science Conference. pp. 549–567.
- Lofgren G. E. and Donaldson C. H. 1975. Curved branching crystals and differentiation in comb-layered rocks. *Contributions to Mineralogy and Petrology* 49:309–319.
- Lofgren G. E. 1980. Experimental studies on the dynamic crystallization of silicate melts. In *Physics of magmatic processes*, edited by Hargrove R. B. Princeton: Princeton University Press. pp. 487–541.
- Lofgren G. E. 1989. Dynamic crystallization of chondrule melts of porphyritic olivine composition: Texture experimental and natural. *Geochimica et Cosmochimica Acta* 53:461–470.
- Maddock R. H. 1983. Melt origin of fault-generated pseudotachylytes demonstrated by textures. *Geology* 11:105–108.
- Mandelbrot B. B. 1983. *The fractal geometry of nature*. New York: W. H. Freeman. 468 p.
- Marsh B. D. 1998. On the interpretation of crystal size distributions in magmatic systems. *Journal of Petrology* 39:553–599.
- McSween H.Y., Jr. and Jarosewich E. 1983. Petrogenesis of the Elephant Moraine A79001 meteorite: Multiple magma pulses on the shergottite parent body. *Geochimica et Cosmochimica Acta* 47:1501–1513.
- Melosh H. J. 1985. Ejection of rock fragments from planetary bodies. *Geology* 13:144–148.
- Meyer C. 2004. Mars Meteorite Compendium NASA Johnson Space Center, Houston, <http://www-curator.jsc.nasa.gov/curator/antmet/mmc/mmc.htm>.
- Mikouchi T., Miyamoto M., and McKay G. 2001. Mineralogy and petrology of the Dar al Gani 476 martian meteorite: Implications for its cooling history and relationship to other shergottites. *Meteoritics & Planetary Science* 36:531–548.
- Mittlefehldt D.W. 1994. ALH 84001, a cumulate orthopyroxenite member of the martian meteorite clan. *Meteoritics* 29:214–221.
- Nishiizumi K., Masarik J., Welten K. C., Caffee M. W., Jull A. J. T., and Klandrud S. E. 1999. Exposure history of new martian meteorite Dar al Gani 476 (abstract #1966). 30th Lunar and Planetary Science Conference. CD-ROM.
- Nishiizumi K., Caffee M. W., Jull A. J. T., and Klandrud S. E. 2001. Exposure history of shergottites Dar al Gani 476/489/670/735 and Sayh al Uhaymir 005 (abstract #2117). 32nd Lunar and Planetary Science Conference. CD-ROM.
- Ohnenstetter D. and Brown D. L. 1992. Overgrowth texture, disequilibrium zoning, and cooling history of a glassy four-pyroxene boninite dyke from New Caledonia. *Journal of Petrology* 33:231–271.
- Ostertag R., Omthauer G., Rager H., and McSween H. Y., Jr. 1984. Fe³⁺ in shocked olivine crystals of the ALH 77005 meteorites. *Earth and Planetary Science Letters* 67:162–166.
- Park J., Okazaki R., and Nagao K. 2003. Noble gas studies of martian meteorites: Dar al Gani 476/489, Sayh al Uhaymir 005/060, Dhofar 019, Los Angeles 001, and Zagami (abstract #1213). 34th Lunar and Planetary Science Conference. CD-ROM.
- Park J., Nagao K., and Bartoschewitz R. 2004. Noble gas studies of the Sayh al Uhaymir 150 martian meteorite (abstract). *Meteoritics & Planetary Science* 39:A81.
- Russell S. S., Zipfel J., Grossman J. N., and Grady M. M. 2002. The Meteoritical Bulletin, No. 86. *Meteoritics & Planetary Science* 37:A157–A184.
- Russell S. S., Zipfel J., Folco L., Jones R., Grady M., McCoy T., and Grossman J. N. 2003. The Meteoritical Bulletin, No. 87. *Meteoritics & Planetary Science* 38:A189–A248.
- Russell S. S., Folco L., Grady M. M., Zolensky M. E., Jones R., Righter K., Zipfel J., and Grossman J. N. 2004. The Meteoritical Bulletin, No. 88. *Meteoritics & Planetary Science* 39:A215–A272.
- Schaal R. B. and Hörz F. 1977. Shock metamorphism of lunar and terrestrial basalts. Proceedings, 8th Lunar Science Conference. pp. 1697–1729.
- Spray J. G. and Rae D. A. 1995. Quantitative electron-microprobe analysis of alkali silicate glasses: A review and user guide. *Canadian Mineralogist* 33:323–332.
- Schmitt R. T. 2000. Shock experiments with the H6 chondrite Kernouvé: Pressure calibration of microscopic shock effects. *Meteoritics & Planetary Science* 35:545–560.
- Stöffler D., Keil K., and Scott E. R. D. 1991. Shock metamorphism of ordinary chondrites. *Geochimica et Cosmochimica Acta* 55:3845–3867.
- Stöffler D. 2000. Maskelynite confirmed as diaplectic glass: Indication for peak shock pressures below 45 GPa in all martian meteorites (abstract #1170). 31st Lunar and Planetary Science Conference. CD-ROM.
- Stolper E. and McSween H.Y., Jr. 1979. Petrology and origin of the shergottite meteorites. *Geochimica et Cosmochimica Acta* 43:1475–1498.
- Walker D. R. J., Kirkpatrick J., Longhi J., and Hays J. F. 1976. Crystallization history of lunar picrite basalt sample 12002: Phase equilibria and cooling-rate studies. *Geological Society of America Bulletin* 87:646–656.
- Wänke H. and Dreibus G. 1988. Chemical composition and accretion history of terrestrial planets. *Philosophical Transactions of the Royal Society of London A* 325:545–557.
- Wiens R. C. and Pepin R. O. 1988. Laboratory shock emplacement of noble gases, nitrogen and carbon dioxide into basalt, and implications for trapped gases in shergottites EET A79001. *Geochimica et Cosmochimica Acta* 52:295–307.
- Zipfel J. 2000. Sayh al Uhaymir 005/008 and its relationship to Dar al Gani 476/489 (abstract). *Meteoritics & Planetary Science* 35:A178.
- Zipfel J., Scherer P., Spettel B., Dreibus G., and Schultz L. 2000. Petrology and chemistry of the new shergottite Dar al Gani 476. *Meteoritics & Planetary Science* 35:95–106.